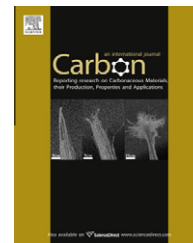


available at [www.sciencedirect.com](http://www.sciencedirect.com)journal homepage: [www.elsevier.com/locate/carbon](http://www.elsevier.com/locate/carbon)

## Review

# Evaluating the characteristics of multiwall carbon nanotubes <sup>☆</sup>

John H. Lehman <sup>a,\*</sup>, Mauricio Terrones <sup>b,c</sup>, Elisabeth Mansfield <sup>d</sup>, Katherine E. Hurst <sup>e</sup>, Vincent Meunier <sup>f</sup>

<sup>a</sup> Optoelectronics Division, Physical Measurement Laboratory, National Institute of Standards and Technology, 325 Broadway, Boulder, CO 80305, USA

<sup>b</sup> Research Center for Exotic Nanocarbons (JST), Shinshu University, Wakasato 4-17-1, Nagano City 380-8553, Japan

<sup>c</sup> Department of Physics, Department of Materials Science and Engineering & Materials Research Institute, The Pennsylvania State University, 104 Davey Lab., University Park, PA 16802-6300, USA

<sup>d</sup> Materials Reliability Division, Materials Measurement Laboratory, National Institute of Standards and Technology, 325 Broadway, Boulder, CO 80305, USA

<sup>e</sup> National Renewable Energy Laboratory, 1617 Cole Blvd., Golden, CO 80401-3305, USA

<sup>f</sup> Department of Physics, Applied Physics, and Astronomy, Rensselaer Polytechnic Institute, 110 Eighth Street, Troy, NY 12180-3590, USA

## ARTICLE INFO

## Article history:

Received 2 December 2010

Accepted 15 March 2011

Available online 17 March 2011

## ABSTRACT

During the past 20 years, multiwall carbon nanotubes (MWCNTs) have become an important industrial material. Hundreds of tons are produced each year. This review is a survey of the scientific literature, motivated by industrial requirements and guidelines for environment, health and safety compliance. Sampling, size, area, density, color, crystallinity, as well as purity compared to properties of non-MWCNT carbon and catalyst metals, are presented. No single measurement tool provides a complete characterization; therefore, we summarize methods that include scanning electron microscopy, transmission electron microscopy (TEM), fast Fourier transform of high-resolution TEM, Raman spectroscopy, reflectance and thermogravimetric analysis. Fourier transform infrared spectroscopy reveals information with regard to functional groups interacting the tube surface. Brunauer–Emmett–Teller (BET) analysis is reviewed as the basis for evaluating specific surface area. We extend the review by presenting taxonomy of defects present in MWCNTs. Finally, we provide an appendix from documentary standards that are pertinent and reasonable for bulk measurements.

Published by Elsevier Ltd.

## Contents

1. Introduction . . . . .	2582
2. Sampling . . . . .	2583

<sup>☆</sup> Publication of NIST, an agency of the US government, not subject to copyright.

\* Corresponding author: Fax: +1 303 497 4286.

E-mail address: [lehman@boulder.nist.gov](mailto:lehman@boulder.nist.gov) (J.H. Lehman).

0008-6223/\$ - see front matter Published by Elsevier Ltd.

doi:10.1016/j.carbon.2011.03.028

3.	Size and shape . . . . .	2585
3.1.	Purity of MWCNTs . . . . .	2585
3.2.	Diameter and length of MWCNTs . . . . .	2585
3.3.	Disorder and crystallinity . . . . .	2587
4.	Optical characterization . . . . .	2587
4.1.	Color . . . . .	2587
4.2.	FTIR spectroscopy . . . . .	2588
4.3.	Raman spectroscopy . . . . .	2588
4.3.1.	Radial breathing mode . . . . .	2589
4.3.2.	Splitting of the G-band . . . . .	2590
4.3.3.	Splitting of the D-band . . . . .	2590
4.3.4.	Using the G'-band to assess MWCNT sample purity . . . . .	2590
4.4.	Summary . . . . .	2591
5.	Surface area . . . . .	2591
6.	Density . . . . .	2592
7.	Thermogravimetric analysis and purity . . . . .	2593
8.	Defects . . . . .	2595
8.1.	Structural defects . . . . .	2596
8.2.	Bond rotations . . . . .	2597
8.3.	Doping-induced defects . . . . .	2597
8.4.	Non-sp <sup>2</sup> carbon defects . . . . .	2597
9.	Concluding remarks . . . . .	2597
	Acknowledgments . . . . .	2598
	Appendix A . . . . .	2599
A.1.	Single-wall carbon nanotube (SWCNT) . . . . .	2599
A.2.	Multiwall carbon nanotube (MWCNT) . . . . .	2599
A.3.	Double-wall carbon nanotube (DWCNT) . . . . .	2599
A.4.	Characteristics of interest . . . . .	2599
A.5.	Partial list of regulatory requirements in the US . . . . .	2599
	References . . . . .	2599

## 1. Introduction

Twenty years ago, Iijima reported the structural morphology of multiwall carbon nanotubes (MWCNTs) by use of a high-resolution transmission electron microscope (HRTEM) and electron diffraction. On this anniversary, we review two decades of measurement techniques, analysis and results that characterize the intrinsic properties of MWCNTs [1].

Our emphasis is primarily bulk measurement and characterization results that distinguish among different types of MWCNTs. For example, if presented within a pile of soot from a chemical (ethane) vapor deposition (CVD) process, how does one identify MWCNTs in the mix? Without knowledge *a priori*, how does one distinguish MWCNTs from single-wall carbon nanotubes (SWCNTs)? Such information is useful for the inherent technical information from which to make economic and engineering judgments, but also for compliance with possible environment, health and safety (EH&S) requirements. From an informal survey of vendor literature, vendor websites and verbal discussions, measurement results of interest include: color, size (inner diameter, outer diameter, length, number of shells), purity (with respect to non-nanotube carbon, ash and catalyst), type of defects, topology

and surface area. No single measurement tool provides a complete characterization and none is entirely quantitative. Therefore, we create a profile of our pile of soot from an ensemble of measurement techniques including optical spectroscopy, Raman spectroscopy, electron microscopy, mass, volume and gas adsorption. In addition, we add measurement analysis as adjuncts to these tools such as fast Fourier transform (FFT) analysis of high-resolution transmission electron microscopy (HRTEM), linewidth vs. intensity of Raman scattering, and BET analysis of gas adsorption.

The MWCNTs observed by Iijima were produced at extremely high temperatures (near 3500 °C) by use of an arc discharge between graphite electrodes [1]. Today MWCNTs are produced industrially at much lower temperatures (near 700–950 °C) via the catalyst-based chemical vapor deposition (CVD) process developed by Endo and coworkers in the 1970s [2]. In 2011, the outlook for commercial use of carbon nanotubes is favorable. Hundreds of tons of MWCNTs are produced each year and in far greater numbers than SWCNTs [3]. Compared to SWCNTs, however, we find fewer research papers relevant to distinguishing MWCNTs from other carbon allotropes.<sup>1</sup> Ma-Hock et al. recently reported from a 3-month study of rats that inhalation exposure to MWCNTs produced

<sup>1</sup> Publications about SWCNTs outnumbered those about MWCNTs by nearly 10 to 1, while in terms of industrial production by mass, MWCNTs outnumbered SWCNTs 10 to 1.

no systemic toxicity [4], however, this is only one citation among thousands that have been and will be pertinent. In addition, regulatory requirements will continue to evolve. From an overview of regulatory requirements in the US and elsewhere, we find that the following measurements and characteristics are of interest:

- (1) Type of multiwalled carbon nanotube (concentric cylinders, stacked cups or scrolled tubes; number of walls/tubes).
- (2) Configuration of nanotube ends (e.g., open, capped).
- (3) Description of any branching.
- (4) Width/diameter of innermost wall/tube (average and range).
- (5) Carbon unit cell ring size and connectivity.
- (6) Morphology of nanotube along the long axis (straight, bent, buckled).
- (7) Preferred hexagonal array orientation within the tubes along their axes.
- (8) Particle size of catalyst used in the manufacture of the nanotube.
- (9) Molecular weight (average and range).<sup>2</sup>
- (10) Particle properties: shape, size (average and distribution), weight (average and distribution), count, surface area (average and distribution), surface-to-volume ratio, aggregation/agglomeration.
- (11) Structural defect content (non-carbon impurities or dopants, lattice defects, adsorbed molecules, etc.).

There is a great deal of work that we will not address in this review and other matters that simply point to the need for future work. We do not present a comprehensive theoretical review, but discuss theoretical considerations as necessary. Molecular dynamics or density functional theory modeling is difficult, based simply on the large number of atoms required to model the multi-shell system, and the difficulty of accurately describing non-bonding interactions between individual shells [5]. We do not address electrical or electronic or thermal transport properties, nor do we address thermodynamic theory for growth and formation of MWCNTs [6]. Our emphasis is that of bulk properties, but one could consider the matter of a large individual MWCNT behaving as a 'bulk' material [7,8]. Thus we have organized the review along the lines of sampling, size, shape, defects, optical properties, surface area, density and purity. These categories are not mutually exclusive. For example, it is difficult to discuss purity without discussing Raman, but TGA is arguably the most popular tool to establish batchwise purity of bulk MWCNTs.

## 2. Sampling

MWCNTs can occur as a byproduct of natural and industrial processes. For example, MWCNTs have been found from forest fires and from household cooking with propane and natural gas stoves [9,10]. This observation was carried out by use

of TEM while searching small samples taken from large quantities of soot. Although MWCNTs occur naturally, we believe that contamination of laboratory samples from environmental sources is unlikely. Sampling for occupational exposure and safe handling is also outside the scope of this review. The difficulty of obtaining reproducible and statistically valid samples in the most favorable laboratory conditions suggests that the job of the regulator or compliance officer is daunting. For example, will a layer of well dispersed and potentially more hazardous nanomaterial become aggregated micromaterial when swabbed? From the point of view of laboratory investigations and industrial use, sampling depends on the measurement of interest. Just as no single measurement is sufficient to fully characterize MWCNTs, no single form of sample preparation is suitable for the various measurement platforms.

MWCNTs are usually hydrophobic, so they are not readily dispersed in water. Sonication is useful, but without the addition of a surfactant, MWCNTs will fall out of water suspension within minutes. Unfortunately, the properties of the surfactant must be considered along with the intrinsic properties of the MWCNTs. Organic solvents (for example, toluene, chloroform, acetone, methanol and ethanol) are commonly used, but no accepted standard method of dispersion in solvent exists to our knowledge. Typical dispersions are on the order of micrograms of MWCNTs per milliliter of liquid. For spectroscopy, in lieu of dispersion in a cuvette, MWCNT samples can be airbrushed [11], drop cast or spun on a transparent slide. Volatile material evaporates, but in the case of surfactant based solutions, the residue must be considered with any analysis. Nanotube films (or bucky paper) can be prepared from solution by drawing dispersed material through cellulose or Teflon filters [11]. The remaining bucky paper is well suited for Raman spectroscopy in the backscattering configuration, reflection spectroscopy and SEM.

Krause et al. studied sedimentation behavior under centrifugation forces of carbon nanotube (CNT) materials produced at different synthesis conditions. The CNT material was dispersed in aqueous surfactant solution and the extent of dispersion was correlated with optical spectroscopy as shown in Fig. 1 [12–14]. Similar results are reported for ultraviolet and visible absorption spectra of SWCNTs by Grossiord et al. [15]. At the beginning of sonication, MWCNTs exist as aggregates and bundles in suspension and in this form, no exceptional features are seen in the ultraviolet or visible spectrum. With sufficient sonication energy to overcome van der Waals attractions among adjacent tubes, disentanglement and greater dispersion follows, and correlates with more apparent spectral features such as the appearance of the  $\pi$ -plasmon peak.

FTIR measurements are typically undertaken with nanotubes mixed with potassium bromide and pressed into a pellet. Unwanted residual water or carboxyl functionalization may remain. Osswald et al. describe heating sample pellets for 24 h at near the boiling temperature of water, and assume

<sup>2</sup> This may be a poorly posed question. For example, fullerenes ( $C_{60}$ ,  $C_{80}$ ) have a molecular weight based on a well-defined number of atoms. But what about MWCNTs;  $C_n$  where  $n = ?$ .

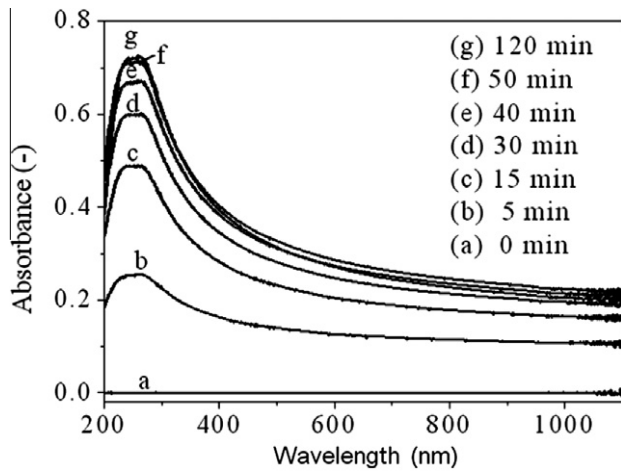


**Fig. 1 – Evolution of optical properties of MWCNTs with respect to sonication attributed to aggregates and bundling of the bulk material [14]. Reproduced with permission from Elsevier.**

that O–H vibrations originate from water in the sample rather than from the functional groups that may be attached to the MWCNTs [16].

Sample preparation for TGA requires 3–10 mg of dry powder for a single measurement, with multiple independent samples or larger samples being necessary to achieve statistically valid assessment, particularly with respect to metal content [17]. The method of applying airbrushed, drop cast or spun-on samples on a quartz crystal microbalance has also been documented as a method of TGA-like measurements [18].

Caplovicova reviewed several common methods for TEM sample preparation including an ultrasonic method, a cutting method and ion thinning. Caplovicova's method is a so-called replica method that is intended to provide the best representation of as-produced material without alteration. The most common method is arguably the ultrasonic method, whereby a sample of MWCNT material is scraped into a solution of organic solvent (ethanol, methanol or acetone), sonicated and dropped onto lacey carbon or copper grid. A shortcoming of

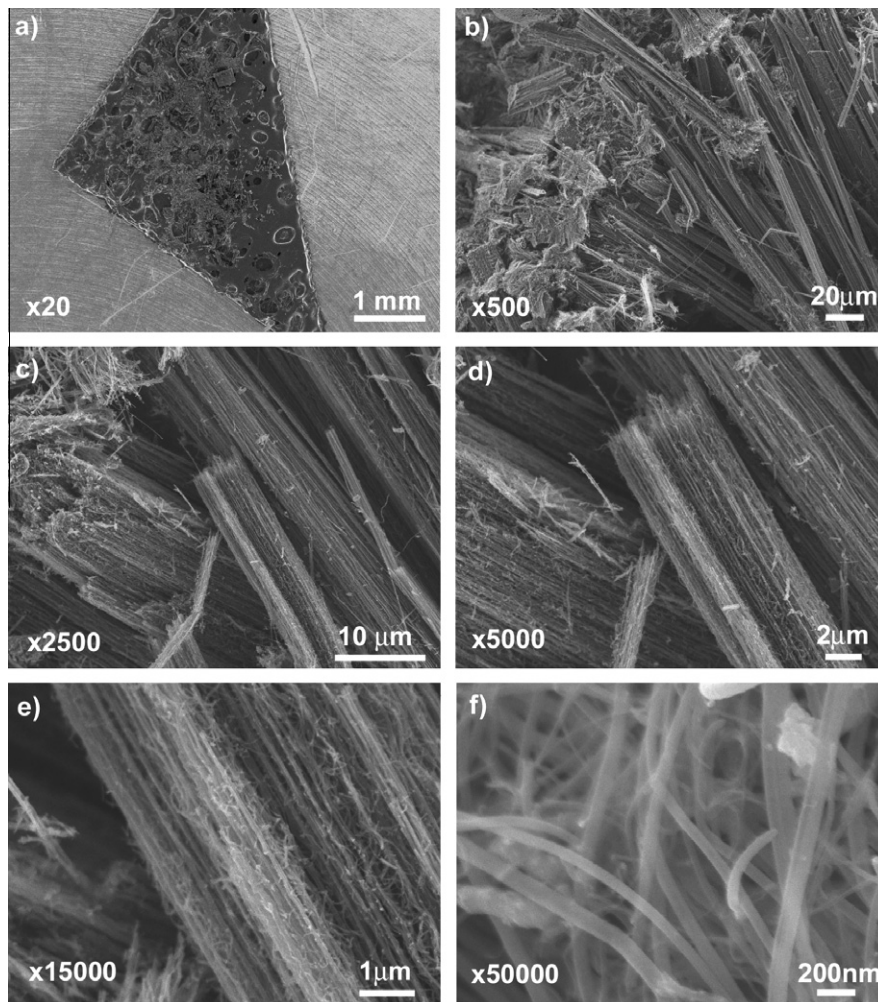


**Fig. 2 – SEM images of a nanotube sample produced by CVD process (nanotube area defined by triangular carbon tape in (a)). The images were recorded at different magnifications in order to visualize the overall sample and the morphology of the tubes and way they are arranged. In this case, the sample contains bundles of aligned nanotubes (or nanofibers), and the amount of unwanted particles is relatively small.**

this method is that the combination of solvent and sonication may alter the nature of the sample by removing residual catalyst or by damaging the tubes' structure [19].

For a method to determine apparent density, we found a documentary standard that applies broadly to organic polymers and powders. EN ISO 60 specifies pouring a sample through a funnel into a measuring cylinder of 100 cm<sup>3</sup> capacity, removing the excess with a straightedge, and determining the mass of the contents. The apparent density is expressed in the units of grams per milliliter.

### 3. Size and shape

Among the most common tools to characterize the morphologies and dimensions of *as-produced* MWCNTs (in powder form), scanning electron microscopy (SEM) is by far the most popular. The advantage of SEM over other microscopy techniques is the fact that it is simple and could be carried out routinely. At the present, SEM imaging is used to characterize the overall morphology of MWCNT samples, and could also be used to quantify the degree of purity within samples, as well as the dimensions of the tubules, as shown in Fig. 2.

#### 3.1. Purity of MWCNTs

By quantifying the percentage of unwanted materials per unit area within the sample SEM images, it is possible to estimate a degree of purity (for example, 90% tubular material, 5% spherical particles, and 5% irregular objects). Most SEM instruments are able to resolve structures greater than 5 nm in diameter (for example, tungsten filaments), and the most sophisticated SEM can achieve point resolutions less than 1 nm (field emission microscopes with monochromators). However, since most of the MWCNTs synthesized at present exhibit diameters greater than 5 nm, tungsten-tip instruments are sufficient for carrying out morphological characterization. In order to establish standards in the overall characterization, we suggest recording of SEM images at incremental magnifications: 20 $\times$ , 500 $\times$ , 2500 $\times$ , 5000 $\times$ , 15,000 $\times$  and 50,000 $\times$ . In this way, it is possible to estimate the overall morphology of the MWCNT sample. For example at 20 $\times$  and 500 $\times$ , one could determine whether the powder sample consists of tube bundles, entangled tubular objects, round agglomerates, tubular-and-particle agglomerates, irregular agglomerates, etc. At 2500 $\times$  and 5000 $\times$ , it is possible to quantify the overall surface occupied by tubular objects and by non-tubular objects, in order to determine a degree of purity within the powder samples. Lower uncertainty could be obtained if at least 5 SEM images with the same magnification are analyzed and fully quantified. It may be expedient to develop imaging algorithms that are able to quantify and differentiate tubular from irregular objects (per unit area). Beam energy for either tungsten filament or field emission SEM is critical, yet no standard specification exists that we are aware of. When using a tungsten filament SEM, a recommended voltage in order to avoid possible charging effects and achieve better image contrast within the nanotube samples would be 10 and 2 keV (or less) for a field emission SEM. The reader should be aware that operation voltages for tungsten filament

SEM or field emission SEM usually range from 1 and 30 keV, and according to the experience of the authors, we are providing values for recommended practice that could be used for characterizing MWCNTs samples in the future. From low magnification TEM images (e.g., 20,000–50,000 $\times$ ), one can estimate the purity of the sample by quantifying the number of tubes and irregular objects per unit area (just as for SEM).

#### 3.2. Diameter and length of MWCNTs

The diameters of MWCNTs could be roughly estimated from SEM images recorded at magnifications of greater than

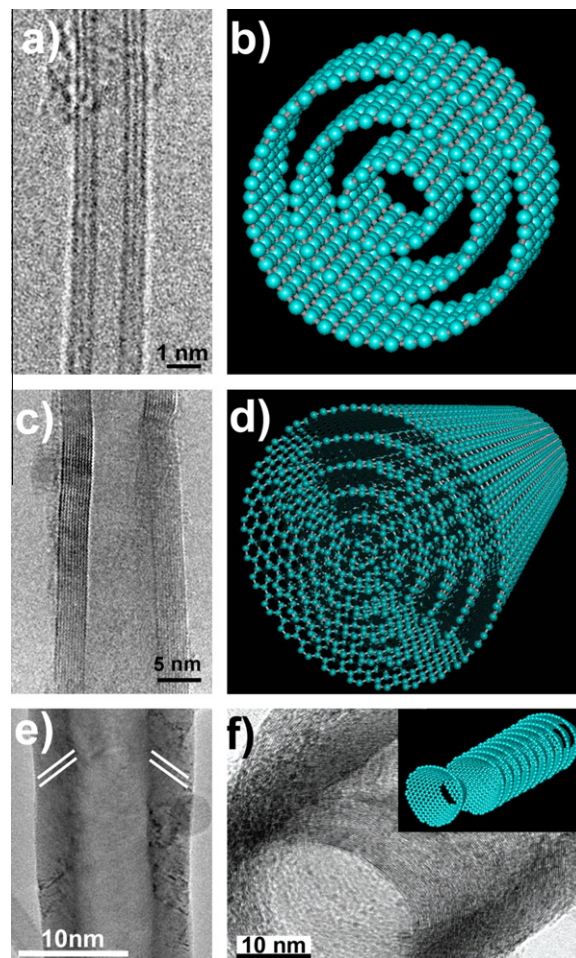


**Fig. 3** – Images of tubular carbon materials and molecular models representing their morphology. (a) Triple-walled carbon nanotube and (b) molecular model of a triple-walled carbon nanotube; (c) HRTEM of a multi-walled carbon nanotube consisting of 10 nested tubules; (d) molecular model of a six-walled carbon nanotube; (e) TEM image of a stacked cone nanofiber consisting of open cones that are piled up; (f) cross-section of a cup-stacked carbon nanofiber with inset representing the molecular model of the nanofiber. Note that the herringbone-type nanofiber seems similar to the cup-stacked but the former consists of scrolled graphene ribbons forming helically coiled cones. According to the Endo et al. [22], (e) and (f) consist of stacked cones but further studies are needed. (Images courtesy of T. Hayashi and M. Endo.)

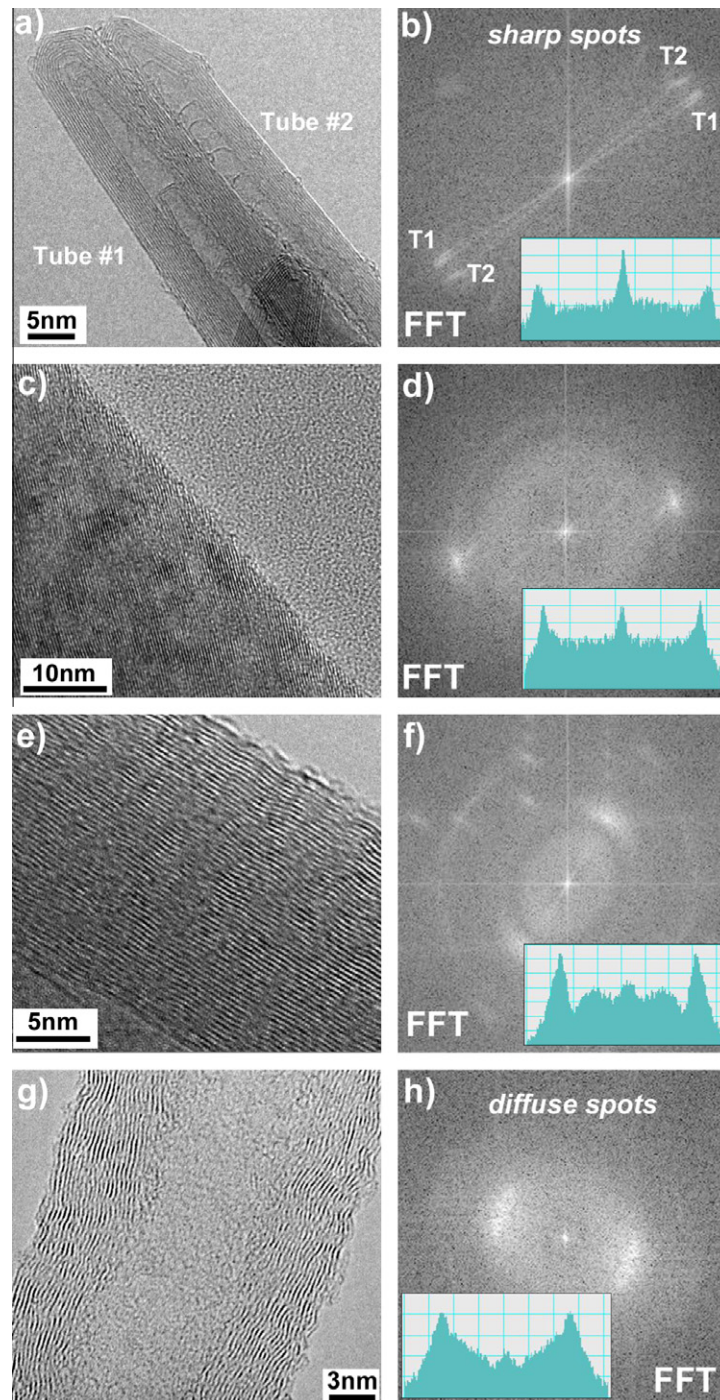


Fig. 4 – HRTEM images of different carbon nanotubes and their corresponding fast Fourier transform (FFT). The tubes exhibit different degrees of crystallinity and this degree could be monitored by analyzing the nature and appearance of contrast (spots) in the FFT image: (a) HRTEM image of two MWCNTs that have been produced via the arc-discharge experiments, revealing an extremely high degree of crystallinity; (b) the FFT displays two sharp pairs of spots and the line scan along one of the pair (inset) confirms the presence of sharp spots corresponding to highly ordered carbon (narrow peaks); (c) HRTEM image of a cup-stacked carbon fiber showing a relatively high degree of crystallinity; (d) The FFT shows the presence of narrower peaks, and the line scan confirms the presence of a highly ordered carbon; (e) HRTEM of a MWCNT produced by the CVD method and the FFT showing a medium degree of crystallinity; note that the FFT (f) displays more diffuse spots associated with the (0 0 l) planes; (g) HRTEM image of a poorly crystalline MWCNT exhibiting numerous imperfections. The line scan reveals a rather poor crystallinity caused by the presence of wide peaks and low intensity of the central spot; this is a characteristic of defective CNTs exhibiting distorted layers that form the concentric nanotubes.

20,000 $\times$ . A representative average value and distribution of diameters may be obtained from multiple, independent SEM images. (We recommend compiling the diameters of at least 250 tubes.) Smaller MWCNTs are found at the lower limit of resolution of SEMs, which falls in the range of 1–20 nm. Therefore, estimating tube diameter and tube-diameter distribution is SEM dependent. Corroboration by TEM is recommended. The outer-surface morphology of MWCNTs can be characterized by SEM and this technique also could be coupled with TEM analysis. In order to identify the inner morphology of MWCNTs, it is necessary to use transmission electron microscopy (TEM) and high-resolution TEM (HRTEM). Tube length can be estimated if the tubes are straight and distinguishable. However, if the tubes are entangled, additional sample preparation (greater dispersion, for example) should be undertaken. One could also estimate the overall diameters of tubes from low-magnification TEM images taken at 100 $\times$ –200 K. An example of this is shown later in Fig. 8.

### 3.3. Disorder and crystallinity

HRTEM is a complementary tool that could be used in specific cases to determine the way the tubular structures are arranged (for example, concentric or nested tubes, scrolled sheets, stacked cup arrays, herringbone-type, etc.) as illustrated in Fig. 3. In addition, by use of HRTEM it is possible to estimate the inner and outer diameter distributions of the concentric tubes [20]. In this instance we recommend that at least 250 independent tubes are measured from a homogeneous sample. It is also important to define the difference of a nanotube and nanofiber. In general, we propose that a nanotube could be defined as a fully hollow fiber with no obstruction, whereas a nanofiber is defined as tubular structure with the partial (bamboo-type) or complete obstruction of the inner tubular cavity. A herringbone structure consists of scrolled graphene ribbons forming helically coiled cones, leaving a full hollow core which could be consistent with the definition of tube and not a fiber.

Finally, HRTEM could be a very useful tool to identify the degree of crystallinity of MWCNT material, as well as the presence of amorphous carbon coating the outer layers of the tubes [20]. We propose that the extent of crystallinity can be established by calculating the fast Fourier transform (FFT) of one segment of a tube under HRTEM. If the FFT consists of sharp spots (narrow peaks), as shown in Fig. 4, the material is highly crystalline. However, if the FFT consists of blurred spots (broad peaks), the material is not highly crystalline. Of course, this approach requires some agreement regarding the focus of the HRTEM image in the first place. Additional work regarding the establishment of a parameter based on the sharpness of FFT of tube walls is still needed. For example, the images taken to calculate the FFT must be carefully focused, yet with minimal beam exposure at high voltages. One can avoid damaging a MWCNT with HRTEM voltage less than 86 keV. At higher operating voltages, say greater than 120 keV, the electron beam irradiation is capable of severely damaging the walls of the tubes [21]. It might be shown that a standardized amorphous substrate on which the MWCNTs are placed could establish the extent of focus (and its characteristic FFT).

Besides the use of FFT on TEM or HRTEM images, one could also analyze selected area electron diffraction (SAED) patterns, using a TEM. Information regarding the degree of crystallinity and tube chiralities within the nested structures is possible using this technique. However, SAED patterns may be more time consuming, but in summary both techniques could be used to estimate the overall crystallinity of MWCNTs.

## 4. Optical characterization

Optical characterization reveals information regarding color, purity, defects and other properties; all of which overlap other areas of this review. We segregate optical characterization by color (including reflectance spectroscopy) and Raman spectroscopy.

### 4.1. Color

The apparent color of MWCNTs is black. But qualities of color, or reflectance with respect to wavelength, depend on topology

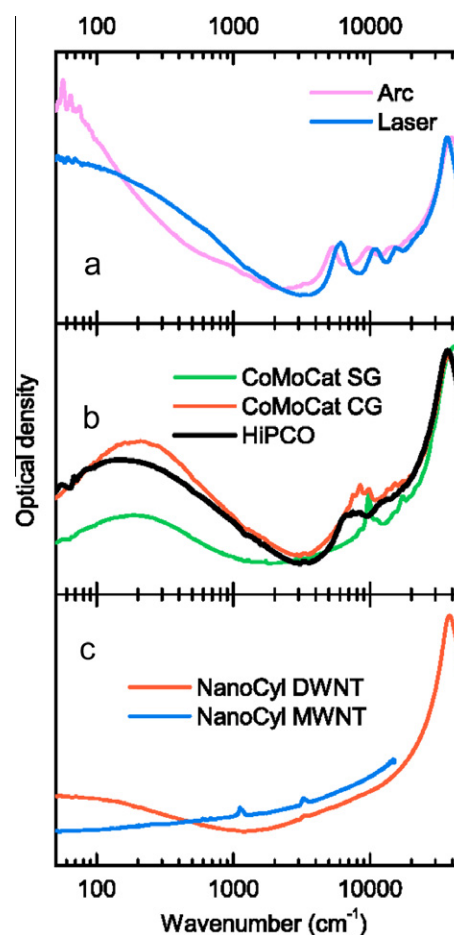


**Fig. 5** – Comparison of optical density of several types of carbon materials for comparison with MWCNTs: (a) arc and laser generated SWCNTs, (b) SWCNTs produced commercially by combustion CVD (CoMoCat) and carbon monoxide disproportionation (HiPCO), (c) DWCNTs compared with MWCNTs. Wiley-VCH Verlag GmbH & Co. KGaA. Reproduced with permission [23].

and electronic structure. In this way, MWCNTs are very different from SWCNTs, and measurably different from graphite and amorphous carbon. Notably, SWCNTs have structure in the visible and near infrared spectrum that we associate with excitonic transitions and increasingly large reflectance in the infrared at wavelengths greater than  $4\ \mu\text{m}$  [23,24]. Kamaras et al. have published extensively, as shown in Fig. 5 on optical properties of nanotubes, and present contrasting spectra of MWCNTs, DWCNTs and SWCNTs made by different processes [23].

The absorbance of MWCNTs in bulk is characterized by a  $\pi$  plasmon with a peak near  $5\ \text{eV}$  ( $248\ \text{nm}$ ). This is not unique to MWCNTs, as it is also seen in SWCNTs and graphite. The reflectance is spectrally uniform in the visible through the infrared. There appears to be a dearth of measurement results indicating the optical properties of MWCNTs, compared to SWCNTs.

Unlike SWCNTs, the optical spectrum in the visible and near infrared in MWCNTs will not depict the chiral angle of the outer shell or radius or length of the carbon nanotube. As we expect from Raman spectroscopy, and simply by virtue of the anisotropic structure of the nanotube, the optical properties depend strongly on the polarization orientation with respect to applied field or nanotube position [25]. Saito et al. in early work describing concentric tubules, found that some of the energy bands of the inner and outer shells are coupled to each other but, because of symmetry, the energy bands of metallic monolayer tubules remain metallic [26]. The implication is twofold: there is tube–tube interaction, and in some cases the optical properties appear as metallic. Brennan et al. reported photoluminescence from MWCNTs despite their expectation that the optical excitation and emission of semiconducting shells would decay non-radiatively in the presence of adjacent metallic shells [27]. Infrared and Raman spectroscopies are complementary to the extent that one relates to dipole moment, while the other relates to polarizability; however, the infrared spectroscopy is even less revealing than the Raman features described previously. Musso et al. published a comprehensive work depicting measurement results following functionalization. This work includes XPS, EDS, Raman, FTIR, BET, TGA, SEM, and TEM. The FTIR is not very informative with respect to identifying organic groups other than carboxylic [28].

#### 4.2. FTIR spectroscopy

FTIR is commonly used to investigate functionalization, which one could also consider under the heading of defects discussed in Section 8. The extent of functionalization will alter the wettability of the nanotubes in various surfactants and may thus also alter the toxicity. Osswald et al. presented two dominant peaks;  $1600$  and  $3450\ \text{cm}^{-1}$  (associated with O–H) and show another at  $1445\ \text{cm}^{-1}$ . Misra et al. identified this peak at  $1445\ \text{cm}^{-1}$  as unique to MWCNTs [29]. Kouklin et al. studied MWCNTs of  $60\ \text{nm}$  diameter and reported spectrally uniform IR spectrum with a  $100\ \text{meV}$  bandgap and IR-active peaks at  $1725\ \text{cm}^{-1}$  (COOH groups),  $1584\ \text{cm}^{-1}$  (G-band),  $1200\ \text{cm}^{-1}$  (D-band) and several peaks in the range of  $3000\ \text{cm}^{-1}$  range that were attributed to  $\text{CH}_x$  groups [30].

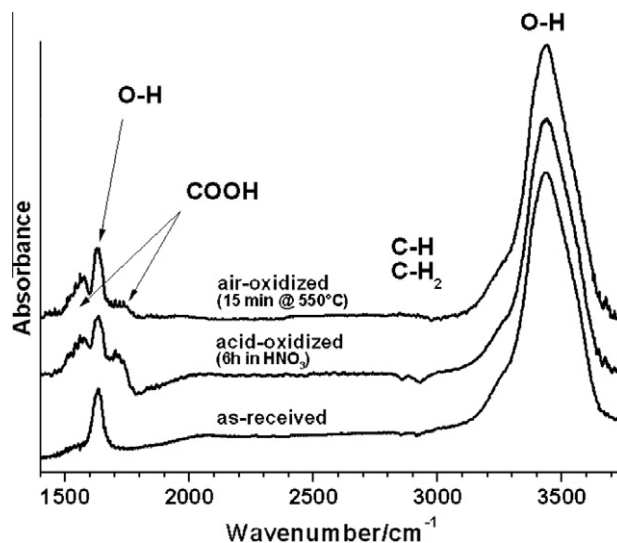


Fig. 6 – FTIR spectra of three types of MWCNTs with functional groups assigned. Wiley-VCH Verlag GmbH & Co. KGaA. Reproduced with permission [16].

Garcia Vidal et al. presented a robust model for the dielectric function of nanotubes developed from use of intrinsic polarization-dependent properties of graphite and treating the tube in two separate cases; a cylinder and a hollow cylinder [31]. The optical properties of graphite have been documented extensively and may be described as a birefringent material. Thus, macroscopic optical properties of MWCNTs will also be constrained by tube orientation with respect to the direction of beam propagation, that is, tubes aligned with the tube axis perpendicular or parallel with respect to the electric field of incoming radiation. Garcia Vidal provided a theoretical basis for this developed from Maxwell's equations. This treatment considers the tube spacing and fill factor in an effective-medium approximation. Qualitatively, the color of a mat of tubes appears similar to that of graphite. A vertically aligned mat of tubes can be quite black, and Yang et al. have presented this as material having absorption greater than any other on record [32]. Mizuno et al. have extended this result from visible wavelengths to  $200\ \mu\text{m}$  [33]. A mixed pile of tubes appears somewhere between graphite and extremely black. Lehman and Theocharous et al. have reported the absorbance of a mat of tubes to have spectrally uniform absorbance in the range of  $0.85$ – $0.95$  in the visible and near infrared [34]. The appearance, as a departure from the IR spectra of graphite, then is attributable to morphology of the mixture, which depends on the length, straightness, bundling and presence of carbon and non-carbon impurities [25] (Fig. 6).

#### 4.3. Raman spectroscopy

Raman spectroscopy yield information about the purity, defects and tube alignment, and assists in the distinction the presence of MWCNTs relative to other carbon allotropes. The technique has been strikingly successful at describing the structural properties of SWCNTs [35]. Unfortunately, the interpretation of the spectra from a MWCNT is often very

complicated and has not yet yielded the same level of output as Raman spectroscopy has achieved for SWCNTs. For Raman scattering, MWCNTs can be said to be an ensemble of carbon nanotubes with diameters ranging from small to very large [35]. Despite this, a number of reports have indicated that Raman spectroscopy can have qualitative and even quantitative characterization power. Because much less theoretical work has been devoted to understanding the Raman spectrum of MWCNTs, the interpretation of the experimental spectra is usually based on well-established results obtained for SWCNTs. This approach has proven valuable but has also shown important limitations since a number of effects, absent in SWCNTs, are often found in the spectra of MWCNTs.

The typical spectrum of a SWCNT has the following major features:

- (1) A low-frequency peak ( $<200\text{ cm}^{-1}$ ), assigned to the  $A_{1g}$  symmetry radial breathing mode (RBM). This peak is absent in graphite and is the main signature of a SWCNT. The frequency of this mode depends only on the tube diameter, but the complete description of tube chiral indices can be inferred from resonant Raman measurements by using information tabulated in the Kataura plot for allowed excitations [36]. Because the RBM frequency is inversely proportional to the tube diameter ( $d$ ), the RBM cannot usually be detected for  $d > 2\text{ nm}$ .
- (2) A group of peaks around  $1340\text{ cm}^{-1}$ , called the “D-band”, is assigned to the presence of disorder in graphitic materials. The origin of the D-band in nanotubes is often considered as a measure of “disorder” as in graphite. It was also demonstrated that the D-band was active for nanotubes satisfying a certain chirality due to double resonance conditions [37]. In addition, it is known that the D-band of isolated SWCNTs can be decomposed into two bands whose separation depends upon the incident laser energy.
- (3) A group of peaks in the  $1550\text{--}1600\text{ cm}^{-1}$  range constitutes the G-band. In graphite, a single peak is present at  $1582\text{ cm}^{-1}$  and corresponds to the tangential vibrations of the carbon atoms. This peak is a good measure of the graphitization of the sample. In nanotubes, this G-band is composed of two features (G+ and G–) due to the confinement of the vibrational wave in the circumferential direction. Because the G+ band corresponds to atomic displacements along the nanotube axis, it is independent of the diameter, as opposed to the G– band, which corresponds to circumferential atomic displacements. The G– band has a different line shape for semiconducting and metallic systems.
- (4) A line is present around  $2600\text{ cm}^{-1}$ , it is an overtone or second-order harmonic of the D mode. It is labeled G' or sometimes D\* or 2D. The G'-band is indicative of long-range order in a sample, and arises from a two-phonon, second-order scattering process that results in the creation of an inelastic phonons.
- (5) Some second-order modes are also visible in the  $1700\text{--}1800\text{ cm}^{-1}$ , but have not attracted particular attention, in part because of their relatively low intensity.

Raman spectroscopy on MWCNTs has been focused on exploiting the presence or absence of these bands in the corresponding spectra to infer electronic and structural information about the tube. In many samples of MWCNTs, the G-band's frequency and lineshape are comparable to those of the  $E_{2g}$  phonon of graphite (though graphite linewidth is typically smaller than that for MWCNTs). The linewidth is, however, not a reliable criterion to distinguish MWCNTs from graphite, since the linewidth may be affected by a number of factors such as tube diameter. The signature of a single-shell vibration is expressed by the presence of a low-frequency RBM and in the splitting of the G-band. In most cases, these two effects are not observed in MWCNTs, even for highly ordered samples. The main reason is that the innermost shell in MWCNTs often has a diameter in excess of 2 nm. For such a size range, the RBM's scaling rules derived for SWNTs indicate that the RBM frequency and intensity are not measurable. This also applies to the scaling rules for the G– band. In other words, for shells of small curvature, the electronic properties differ little from those of flat graphite. It follows that typical MWCNT spectra resemble those of graphite and display little or any effect of cylindrical geometries. This also indicates that the spectral feature of this G mode can often be used to distinguish between MWCNTs and SWCNTs: while the G-band is clearly split into two bands in SWCNTs, the G-band is typically made up of a broad asymmetric feature in MWCNTs. This short survey indicates that using Raman spectroscopy to characterize MWCNTs is not as successful as it is on SWCNT. However, the situation is actually not as gloomy as these general comments indicate, and we will now review some of the key observations made for each region of interest to the MWCNT Raman spectra.

#### 4.3.1. Radial breathing mode

While the MWCNT outer sheet curvature is close to that of graphene, their inner sheets are similar to those of SWCNTs. However, the diameter of the innermost shell depends sensitively on the method used for growth. Jantoljak et al. observed a clear signature of the radial breathing modes of MWCNTs with thin inner shells [38]. Zhao et al. also observed a number of Raman-active peaks in the low-frequency region ( $100\text{--}600\text{ cm}^{-1}$ ) in MWCNTs. Their polarized Raman spectra confirmed that these modes correspond to RBMs that originate from the narrow innermost tubes. The scaling rule for SWCNTs permitted the assignment of the peaks to two tubes embedded inside the MWCNT, in agreement with high-resolution transmission electron microscopy results [39,40]. Note that this technique allowed for the unambiguous detection of the smallest ever detected tube with a diameter of  $d = 0.6\text{ nm}$  at a RBM frequency of  $787\text{ cm}^{-1}$  [41].

Note that the typical analysis of RBMs in MWCNTs is often restricted to the theory developed for isolated SWCNTs. Notably, Lefrant and coworkers developed a model showing that van der Waals interactions between tubes significantly couple modes from adjacent walls. In their bond polarization theory, these authors found that in N-shelled MWCNTs, the N radial breathing modes of the isolated shells lead to N new modes, which are upshifted compared to the breathing vibrations of

the isolated tubes. The model also indicates that the intensity of the modes decreases quickly with increasing diameter and essentially vanishes when the inner diameter exceeds 2 nm, thereby confirming experimental observations [42–44]. A histogram of tube sizes based on a Raman analysis and corroborated by TEM imaging was reported by Benoit et al. as shown in Fig. 8 [45]. Donato and coworkers have published extensively on features observable below  $500\text{ cm}^{-1}$ . In this case, the Raman modes are not related to RBMs of innermost tubes but rather to the presence of defects and the presence of iron catalyst in MWCNTs [46,47].

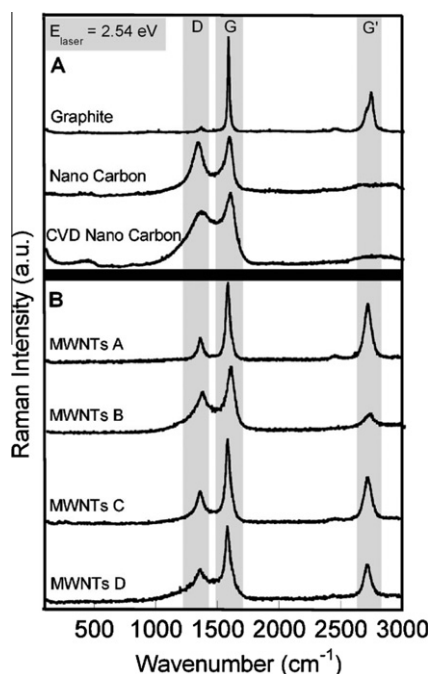
#### 4.3.2. Splitting of the G-band

A single peak of the RBM mode and a multiple splitting of the tangential stretching G-band modes were identified by use of surface-enhanced Raman scattering (SERS) on an individual  $\text{H}_2$ -arc discharge MWCNT. The presence of the RBM is related to the presence of an innermost tube with a diameter of  $\sim 1\text{ nm}$ . SERS results were understood by assigning a G-band modes (linewidth  $4\text{ cm}^{-1}$ ) from the innermost tube and a graphite-like mode (linewidth  $\sim 20\text{ cm}^{-1}$ ) from the outer cylinders in the MWCNT. This observation contrasts clearly with a number of observations of an asymmetric and broad G-band and it demonstrates that MWCNTs possess characteristic Raman spectra different from other  $\text{sp}^2$  carbon allotropes, as long as the innermost shell has a diameter smaller than  $\sim 2\text{ nm}$  [40,48].

Nanot et al. recently studied double sharp line features (at  $1555$  and  $1574\text{ cm}^{-1}$ ) in the G-band of an individual MWCNT. They found that the G-band was actually composed of four distinct modes. Interlayer interactions are likely to induce a more graphite-like behavior rather than a grapheme-like behavior for the G+ band. It was argued that while these peaks are unambiguously due to first-order processes mediated by optical phonons, their line shape cannot be understood completely in terms of graphene's or graphite's unique peaks [49]. For instance, the graphite G peak located at  $1582\text{ cm}^{-1}$  and the single-layer graphene peak at  $1591\text{ cm}^{-1}$  were not observed, a consequence of a weak interaction between the different shells. The assignment of the different peaks remains a cumbersome task since most of theoretical works have been extensively focused on SWCNTs only. For instance, convincing arguments can be given to assign the presence of the modes to the outer shells or, likewise, to the inner shells. In addition, shell-shell interaction broadens the van Hove singularities, and the large number of shells implies that these singularities are quite close to one another, thereby indicating a myriad of possibilities of weakly resonant conditions corresponding to different shells.

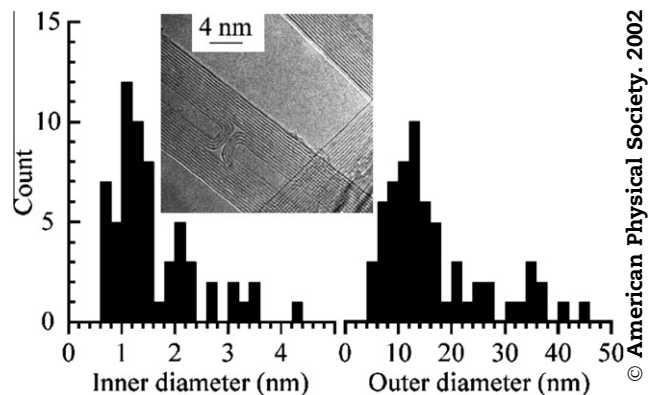
#### 4.3.3. Splitting of the D-band

Gohil and Ghosh measured the Raman spectra of MWCNT deposited on a surface-enhanced Raman scattering (SERS) active substrate and demonstrated the presence of multiple splittings of the tangential mode (G-band), and a splitting of the disorder-induced D-band into two distinct features that are otherwise absent at room temperature [50]. The observation of the D-band splitting indicated that double resonance conditions are satisfied for MWCNTs deposited on a SERS active substrate at low temperature.



© American Institute of Physics. 2007

**Fig. 7 – Revealing features of MWCNTs with respect to purity compared to other carbon structures. Reprinted with permission from [55].**



© American Physical Society. 2002

**Fig. 8 – Summary of MWCNT diameter distributions from Raman analysis corroborated by TEM. Reprinted (figure) with permission from [45, Fig. 2].**

4.3.4. Using the G'-band to assess MWCNT sample purity  
Typical approaches to use Raman spectroscopy for assessment of purity have relied upon the intensity ratio of the D-band peak and the G-band peak. Unfortunately, the interpretation of  $I_D/I_G$  data is not straightforward due to the effect of carbon impurities on these intensities. DiLeo recently published a report where the ratio using the G'-band peak is shown to represent a more accurate alternative for measuring MWCNT quality and purity. The reason for this effect is that since the G'-band results from a two-phonon process, its intensity is particularly sensitive to the sample purity, as disorder would not allow for the coupling effect necessary for the two-phonon process [51]. DiLeo's spectra is reproduced in Fig. 7.

**Table 1 – Summary of spectral features derived from Raman spectroscopy.**

Mode	Designation	Attribute
Sub 500 cm <sup>-1</sup>		Presence of Fe catalyst
Sub 500 cm <sup>-1</sup>		Radial breathing modes. Evidence of MWCNTs with high-purity, low-defect material, thin innermost layers
650 cm <sup>-1</sup>		Appears following intense laser irradiance
1350 cm <sup>-1</sup>	D	Attributable to the presence of disordered amorphous carbon; double resonance effects in sp <sup>2</sup> carbon [58]. The frequency of the D-band peak increases with increasing laser energy. Note that this peak results from amorphous carbon, not defects, in the tube walls [59,60]
1590 cm <sup>-1</sup>	G	This band corresponds to the tangential vibrations of the graphitic carbon atoms. In graphite, a single peak is present at 1582 cm <sup>-1</sup>
1617–1625 cm <sup>-1</sup>	D'	Associated with intercalated graphite compounds (but not graphite), increasing disorder by functionalization and strain in the C–C bond vibrations [56]
1850 cm <sup>-1</sup>		Endo et al. [53] and Fantini et al. [54] proposed a coalescence-inducing mode associated with short carbon chains with an odd number of atoms, interconnecting nanotube surfaces
1855 cm <sup>-1</sup>		Jinno proposes the existence of chainlike carbon materials inside nanotubes [61]
2700 cm <sup>-1</sup>	G'	The G' band is caused by two-phonon scattering around the K point of the Brillouin zone. This mode is known to be sensitive to increasing defect density, but not as significantly as the first-order mode. The mode has significant contributions from regions near the K and M points, yielding peaks at approximately 2700 cm <sup>-1</sup> and approximately 2730 cm <sup>-1</sup> , respectively [56]. The intensity of this peak depends strongly on the metallicity of the nanotube [62]
3240 cm <sup>-1</sup>		Second-order mode of D': increases in intensity with increase in defects in a manner similar to the D' peak at 1617 cm <sup>-1</sup> ; it can be seen as part of the density of states. Defect-induced [56]z

#### 4.4. Summary

In summary, low-frequency Raman modes in MWCNTs can be identified provided the MWCNTs are of high quality and their internal diameter is smaller than 2 nm. These modes originate from the radial breathing modes of the individual walls and are strongly coupled by van der Waals interaction. SERS measurements have also demonstrated the presence of a multiplex G-band spectrum of a MWCNT made of four distinct modes. The relative frequencies of these modes depend strongly on the wall–wall charge transfer, for instance in the presence of a dopant [52], or of an external gate [49]. In addition, low temperature SERS experiments may provide access to certain spectral features of MWCNTs that are otherwise very difficult to see. Finally, note the works of Endo et al. [53] and separately of Fantini et al. [54] who reported a coalescence-inducing mode as a novel vibrational mode at 1850 cm<sup>-1</sup>. This mode is important as it provides a fundamental understanding on how excited nanotubes can in principle be restructured into various nano-morphologies for specific applications.

Endo et al. [53] and separately Fantini et al. [54] reported coalescence-inducing mode as a novel vibrational mode at 1850 cm<sup>-1</sup>. This is based on the observation of linear chains from double-wall carbon nanotubes.

According to Chakrapani et al., the introduction of defects affects all Raman vibrational modes. Chakrapani introduced defects into aligned MWCNTs with plasma etching. Morphological changes observed using Raman spectroscopy were corroborated with X-ray photoelectron spectroscopy (XPS). Chakrapani's analysis of the relationship among the D, D', D', and G modes, however, indicated that no single peak can be used as an accurate standard for estimation of defects [56]. The 2450 cm<sup>-1</sup> feature is the second order feature of

1230 cm<sup>-1</sup> and depends strongly on the structural integrity of the nanotube. Ramadurai et al. documented features at 650 cm<sup>-1</sup> that appear following ever-greater laser irradiance at 1064 nm. While the relative heights of D and G remain unchanged, D' evolves [57] (Table 1).

## 5. Surface area

Many of the unique phenomena of MWCNTs can be attributed to the interactions that occur at the surface. For example, the degree of nanotube dispersion in a composite material is based on the nanotube surface interaction with the surrounding material or solution. Toxicity, gas adsorption, and catalytic activity are also strongly affected by the surface. The effectiveness of nanotube modifications, including purification, change in nanotube bundling, and functionalization, strongly alters the surface area of nanotube samples. Characterization of the nanotube surface area helps to elucidate these interactions and the material activity.

The surface area measurement of carbon nanotubes is most commonly based upon N<sub>2</sub> gas adsorption. The BET (Brunauer–Emmett–Teller) model was developed in 1938, and it is applied to isothermal N<sub>2</sub> adsorption measured at 77 K (liquid N<sub>2</sub> temperature) [63]. It extends the Langmuir adsorption theory to describe multilayer adsorption of N<sub>2</sub> on the surface of a material. BET theory equates the rate of condensation of one monolayer of adsorbate to the rate of desorption of the previous monolayer coverage on the surface. A full description of BET theory and its derivation may be found elsewhere [64,65]. The BET equation is shown in equation 1, where  $n$ , the amount of gas adsorbed, and  $P$ , the pressure, are both measured, while  $P_0$  is the vapor pressure of the adsorbate, and  $n_m$ , the monolayer coverage,

and  $C$  are fitting parameters. The relation shown in Eq. (1) can be expressed as the “linear BET plot” according to Eq. (2).

$$\frac{n}{n_m} = \frac{CP}{(P - P_o) \left[ 1 + (C - 1) \left( \frac{P}{P_o} \right) \right]} \quad (1)$$

$$\frac{\left( \frac{P}{P_o} \right)}{n \left( 1 - \frac{P}{P_o} \right)} = \frac{1}{n_m C} + \frac{(C - 1)}{n_m C} \left( \frac{P}{P_o} \right) \quad (2)$$

From plotting the adsorption data according to the linear BET equation,  $n_m$  and  $C$  can be determined by simultaneously solving the expression for the slope of the line,  $s = (C - 1)/n_m C$ , and the y-intercept,  $i = 1/n_m C$ . This relation is valid only within the linear range of the BET plot, which is typically  $P/P_o = 0.05$ – $0.35$ . In general, adsorption occurring at lower pressures may not be representative of monolayer coverage due to micropore filling, or at higher pressures due to capillary condensation. The value of  $C$  should always be positive, and in general, is attributed to the strength of the interaction between the adsorbate and adsorbent. For more rapid screening, less accurate analysis can be based on a single-point measurement. Provided the analysis is made in the linear region of the BET plot, a single-point measurement for determining the monolayer coverage can be based on Eq. (3):

$$n_m = n \left( 1 - \frac{P}{P_o} \right) \quad (3)$$

The surface area can then be calculated by Eq. (4), based on monolayer absorption coverage ( $n_m$ ), Avogadro's number ( $N_A$ ) and the molecular cross-sectional area of the adsorbate molecule ( $\sigma$ ). The customary value of the cross-sectional area of  $N_2$  is  $0.162 \text{ nm}^2$ .

$$A = n_m N_A \sigma \quad (4)$$

$N_2$  is most commonly used adsorbate for surface area measurement, however,  $N_2$  has a permanent quadrupole that inhibits adsorption on some substrate structures. Alternatively to  $N_2$ , use of a smaller or more spherical adsorbate, such as Ar,  $CO_2$ , He or  $H_2$ , can provide more accurate measurements for surface area. Surface area measurements must be performed at the boiling point of the adsorbate, for example, using Ar as an adsorbate would require the measurement to be performed at liquid Ar temperature. Therefore, the use of other adsorbate molecules is less routine than  $N_2$  since liquid  $N_2$  is more readily available.

There are a number of criticisms of the BET model. The theory is based on homogeneous adsorption sites across the surface. However, for MWCNTs, the adsorption sites are not identical due to bundling/aggregation and/or defects. The BET theory also does not accurately describe the interactions of the adsorbed molecules, and the value for the cross-sectional area of the adsorbate molecule may be modified due to adsorbate–adsorbate or adsorbate–adsorbent interactions. For materials with micropores, pore filling occurs at low pressures prior to complete monolayer coverage, hence the surface area may be over-estimated. Yet if  $N_2$  cannot access the pores for ultra-microporous materials, the surface area may be under-estimated. Therefore, it is recommended that the calculated surface area be denoted as SA (BET). Numerous modifications to the BET equation have been made. However,

despite all of its shortcomings, the BET approach remains a standard method for determining the surface area of MWCNTs.

Peigney et al. have reported a theoretical external surface area of CNTs as a function of their number of walls and diameters to range from 50 to  $1315 \text{ m}^2/\text{g}$  [66]. It was reported to be strongly a function of the number of walls in the nanotube. Experimentally, the measured surface areas for as-produced MWCNTs generally ranges from  $\sim 10$  to  $500 \text{ m}^2/\text{g}$ . Activation or chemical treatments of nanotubes that are employed in purification and processing can result in opening the capped ends of the nanotube ends. This allows access for molecules to adsorb on the inside the nanotube and thus the measured surface area of a MWCNT is no longer the external surface area and may also include the surface area inside the nanotubes. Removing the tube ends has been performed using various chemical and thermal activation methods and the effective surface area has been reported to increase 50–380% after opening the tubes [67–72].

$N_2$  gas adsorption measurements can also be used to characterize the resulting pore size distribution (PSD) created by removing the tube ends. Different models and methods are used to analyze the adsorption data to calculate a PSD, however, this is beyond the scope of the present review. For a good example of PSD characterization for CNTs the reader is referred to Li et al. [73].

## 6. Density

The density of porous materials, such as carbon nanotubes, has several definitions based upon the definition of the material volume. The first definition of density, the bulk density, considers the mass per volume of the material that includes the volume of the pores or void space. For carbon nanotubes, this includes the volume in between nanotube bundles and is dependent upon the geometric configuration or agglomeration of the nanotubes. A second density, the skeletal density, considers the volume of the material that excludes the pore volume. The skeletal (also called the true, apparent or real density) is an intrinsic material property. The packing density is a third type of density, based on the volume of the container in which the material is placed. The packing density is not a material property, but may be an important metric for consumers and manufacturers.

The density of carbon nanotubes is commonly measured by gas pycnometry. With this technique, the sample powder of known mass is placed in a sample chamber and the chamber is pressurized. Next the valve between the sample chamber and an evacuated reference chamber is opened. This change in pressure is compared to the pressure increase observed in the reference cell when the sample cell is empty. Both bulk and skeletal densities can be measured using pycnometry techniques. The bulk density is measured by use of an adsorbate molecule that does not adsorb in the pores of the material. He pycnometry is commonly reported for measuring the skeletal density of carbon nanotubes. Alternatively, the skeletal density may also be calculated based on the atomic spacing within a unit cell measured by X-ray diffraction (XRD) data.

The first experimental study to directly measure the density of MWCNTs was reported in 2009 [74]. Measurements were made on nanotubes that had essentially the same diameter and length, and the researchers employed a differential mobility analyzer and an aerosol particle mass analyzer in series to measure the volume and mass of a CNT. The density was obtained by taking the ratio of measured mass to volume, and it was reported to be 1.74 g/cm<sup>3</sup>. The bulk density of MWCNTs from commercial vendors vary widely, from as low as 0.03 g/cm<sup>3</sup> [75] to as high as 0.22 g/cm<sup>3</sup> [76], while the skeletal density is usually reported to be ~2.1 g/cm<sup>3</sup>.

## 7. Thermogravimetric analysis and purity

No single metric defines nanotube purity. The naive definition of pure MWCNTs in bulk refers to multiple MWCNTs, all identical, each consisting of a specified number of carbon atoms. To the best of our knowledge, no one has found even two MWCNTs that are exactly alike. The idea of sampling grams of such ideal nanotubes, considered pure, is not realistic. For the present discussion purity refers to the nature of the MWCNT content. Impurities would be materials that are other forms of carbon (such as amorphous or graphitic carbons or other structured carbons like SWCNTs or fullerenes), metal impurities, and other chemical species attached to the nanotube (such as nitrogen or boron). An ensemble of measurements including Raman spectroscopy, imaging, thermogravimetric analysis (TGA) and X-ray microanalysis can be used to assess the quality of the sample. The reader is directed elsewhere for a discussion of X-ray microanalysis including energy-dispersive X-ray spectroscopy [77]). Raman spectroscopy and imaging have been already discussed in the broader context. For industrial-scale measurements and batch-to-batch quality control, TGA is arguably the most common and practical tool.

For bulk samples, TGA has been used for quality control of carbon nanotube populations to ensure batch-to-batch homogeneity, from which purity can be inferred if we have confidence from sampling that MWCNTs are present. TGA can be used to evaluate the thermal stability of a material and characterize the purity. The important parameters measured in the weight-loss curve are the initiation temperature, the oxidation temperature, and the residual mass. The initiation temperature is defined at the temperature at which material starts to decompose. The oxidation temperature is defined as the point of maximum weight loss, and is identified as the peak in the derivative of the weight loss as a function of temperature. The oxidation temperature is often defined as the thermal stability of the material. The residual mass is the mass remaining after heating. The residual mass in the TGA of carbon nanotubes is usually attributed to the metal catalyst used to manufacture the nanotubes, as well as the oxidation products of this catalyst. Residual masses can range from nearly 0% to 50%, depending on the quality and homogeneity of the material. The dependence of material quality on residual mass is treated in the context of ash content in documentary standards (the term ash is given to all non-aqueous residue that remains after a sample is burned, and consists mostly of metal oxides. See ASTM D2584, D5630, ISO 3451).

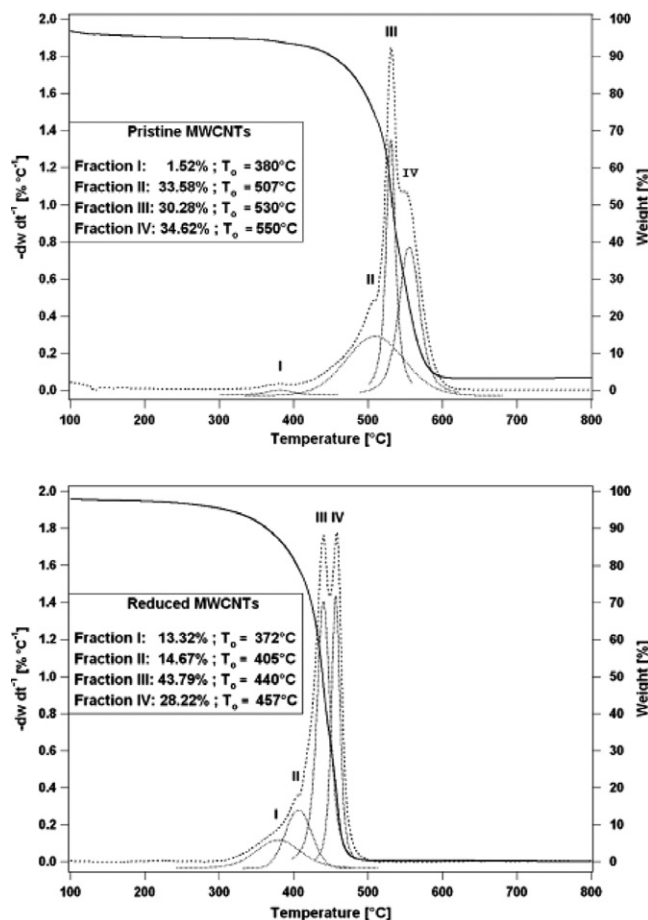


Fig. 9 – TGA curves of the pristine (above) MWCNT and reduced (below) MWCNT sample [81]. Copyright Elsevier (2009).

Highly crystalline MWCNTs have been shown to be more resistant to oxidation compared to other forms of carbon, including diamond, soot, graphite and C<sub>60</sub> [78]. The thermal stability is directly attributed to the aromatic bonding within the MWCNT structure, but can be influenced by the number of walls, the presence and composition of catalyst, the defects within the tubes, and the presence of other materials within the sample (i.e., amorphous carbon, graphitic particles). The derivative of the weight loss curve can often give information about the quality of the material by way of oxidation peaks. An example of the weight loss and derivative of weight loss (multiple peaks) is shown in Fig. 9. The number of oxidation temperature peaks observed is an indicator of material purity. The width of the peak can be used to indicate the purity of the material, with a narrow peak indicating a cleaner material. It is well accepted that amorphous carbons decompose at the lowest temperatures [79,80], followed by SWCNTs, then MWCNTs and graphitic particles, but the oxidation temperature ranges for the different forms of carbon have not been well defined [80]. Oxidation temperatures for MWCNTs vary from material-to-material, but are typically in the range of 400–650 °C. Amorphous carbon contaminates and SWCNTs have lower oxidation temperatures (200–300 °C and 350–500 °C, respectively).

Researchers have attempted to peak fit thermogravimetric data with Gaussian peaks to provide guidance for the types of material present. Scheibe et al. used TGA to investigate a MWCNT material that had been oxidized and reduced as shown in Fig. 9 [81]. Oxidation temperatures for the pristine tubes (350 °C), oxidized (300 °C) and reduced (250 °C) samples suggested that the oxidized samples more closely resemble the pristine tubes, while the reduced tubes have significant defects and functional groups added to the surface. When Scheibe et al. fitted the differential TGA curve, they found an amorphous carbon fraction (Fraction 1, Fig. 9) and three fractions attributed to carbon nanotubes in the pristine sample (Fractions II, III and IV as seen in Fig. 9), compared to four types of carbon nanotubes in the reduced sample (amorphous carbons were considered to be removed during acid reflux; see Fig. 9).

Scheibe et al. demonstrated the complexity of TGA for a well controlled CNT system. With such a complex matrix, there have been many studies to determine the impact of each variable on oxidation temperature.

Many studies of MWCNT have been carried out to demonstrate the differences in MWCNT materials after annealing the CNTs [82–84], oxidation, purification [83,85–87], and post-ultrasonic cutting [88]. In general, annealing improves the degree of crystallinity and strengthens the MWCNT against oxidation, increasing the temperature at which oxidation occurs. Any modification to the nanotube caused by functionalizing the surface or introducing defect sites to the material decreases the oxidation temperature. The influence of size has also been investigated extensively for MWCNTs. The effect of the diameters of MWCNTs on oxidation was compared by Kim et al. [89]. Narrow MWCNTs were found to decompose at lower temperatures than larger-diameter MWCNTs. The length of MWCNTs can influence the decomposition temperature also. Oxidation temperatures have been found to shift to lower temperatures when the length and diameter of MWCNTs decreased [90]. The shift in the oxidation temperature as a result of nanotube diameter has been observed before with other materials. The effects of length are harder to determine, but have been documented for other materials also [88,91].

We expect some correlation between the nature of the catalyst (element, size) and the presence of nanotubes. Not everyone agrees on this relationship. For example, according to Moodley et al., there is no correlation between catalyst particle size and nanotube diameter [92]. According to Ding et al., not all catalyst particles are encapsulated (small particles with diameter less than 2 nm). For those that are encapsulated, the ratio of the number of graphitic layers to the catalyst diameter is approximately 1:0.25 nm [93]. The presence of catalytic particles in MWCNT samples can play a significant role in TGA and has resulted in many papers focused on catalyst concentrations and compositions to improve the nanotube quality. There are many more cases of catalytic composition in the literature [94], but only a short selection of these is presented here. The impacts of the catalyst on the oxidation temperature were investigated for a catalyst containing different weight percentages of Ni [95]. The thermal decomposition occurred in a single step in all cases, with one major mass loss event attributed to

**Table 2 – Catalyst diameter, initiation temperature and oxidation temperature [97]. Copyright Elsevier (2009).**

AB <sub>5</sub> alloy catalyst diameter (μm)	Initial weight loss temperature (°C)	Differential thermal peak temperature (°C)
38–41	544	615
40–50	551	621
50–60	554	628
74–100	618	642
100–150	607	638

MWCNTs. As the Ni content in the catalyst was increased within the sample, the initiation temperature for oxidation decreased. Oxidation temperatures ranged from 540 °C to 600 °C for these materials [95]. The significance of iron content with respect to oxidation and decomposition has been correlated with TGA burn off of MWCNTs [96]. As the iron content of the catalyst increased, the oxidation temperature was also found to decrease. The authors proposed that the decreased reactivity of the CNTs with increasing iron content could be due to a loss of catalytically active sites (due to the decreased presence of catalyst), thus resulting in an increased oxidation temperature [96]. They also proposed that defects in the nanotubes could serve as sites for increased reactivity [96]. Zhang et al. investigated the effects of catalyst size on the oxidation temperature and initiation temperature [97]. They found that the average diameter of their carbon nanotubes increased with the catalyst size. As the catalyst (and nanotube) diameter increased, the initiation temperature and oxidation temperature also increased (see Table 2) for their particular catalyst, which was an AB<sub>5</sub> alloy catalyst, typically used in hydrogen storage applications.

Upon heating, MWCNTs undergo structural changes that have been studied to elucidate the mechanisms of decomposition. The effect of heating was examined by Ajayan et al. [98]. They oxidized nanotubes and stopped mid-oxidation to survey the material by transmission electron microscopy (TEM). When MWCNTs are heated to 800 °C for 10 min, more than 20% have open ends [98]. In the nanotubes where the ends were not open, peeling of the outer layers was seen.

High-resolution TEM studies by Yao et al. supported that oxidation of MWCNTs is initiated at pentagonal defects in the nanotube [99]. The reactivity is due to strain within the tip caused by defects, which induce out-of-plane bending in the graphite sheet, increasing the reactivity at that specific location [98,99,78]. Yao confirmed defects in MWCNTs tips (pentagonal or heptagonal) by microscopy as initiation sites which induce strain in the carbon nanotube, making the MWCNT more susceptible to oxidation [99]. After initiation, MWCNT decomposition occurs. Ajayan et al. observed a thinning of the nanotubes in a layer-by-layer fashion, exactly opposite of the proposed mechanism of growth [98]. Yao found the decomposition rates of concentric layers to be independent of the period during which the layer has been exposed, and showed faster decomposition rates for layers within the nanotube structure (Fig. 10) [99]. Decomposition along the walls was also observed,

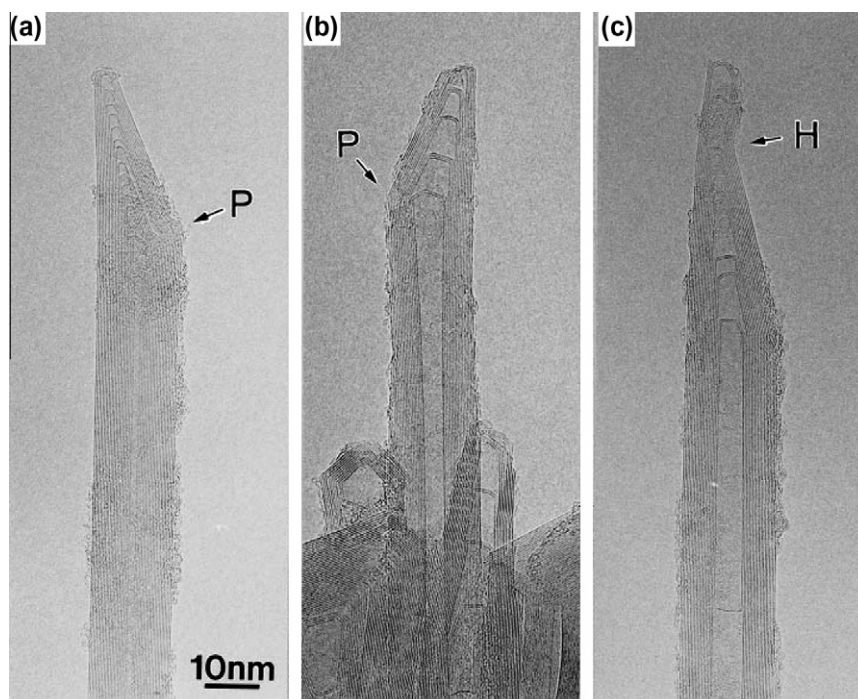


Fig. 10 – HRTEM images of MWCNT with pentagon (P) and heptagon (H) defects. With permission from Yao et al. [99].

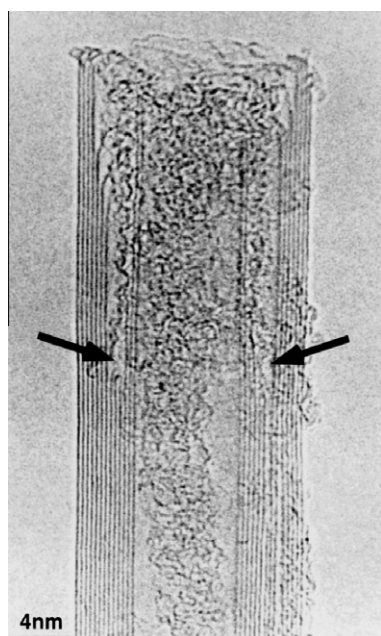


Fig. 11 – HRTEM of an oxidized multiwalled carbon nanotube showing several middle layers that oxidized much faster than both outside and inside layers. With permission from Yao et al. [99].

indicating that defects along the length of the tube may also contribute to decomposition of the MWCNT by providing initiation sites for the decomposition [100]. The decomposition of middle layers faster than interior or exterior layers, and this effect is thought to be due to the helicity of the

nanotubes or the migration of oxygen atoms to defect sites in order to initiate oxidation [99]. (Note that the tubes used by Ajayan, Yao and coworkers contained no catalytic particles because they were produced by the arc discharge of graphite electrodes.)

After the carbon nanotube is open, it begins to fill with carbonaceous debris (see Fig. 11) [98,99]. This process has been attributed to the peeling of inner layers [99] and debris being passively drawn into the carbon nanotube structure [98]. This process must be taken advantage of in order to fill the carbon nanotube with metals [98].

## 8. Defects

Defects are extremely important in determining the physicochemical properties of crystals and nanostructures, including carbon nanotubes. In particular, defects could affect the morphology and functionality of the MWCNTs. Unfortunately, it is extremely difficult to identify accurately and quantitatively the type of defects contained in graphene-like materials, and researchers have not been able to set standards for them or distinguish them systematically. For carbon nanotube systems, the most common defects are (a) vacancies, (b) heptagon–pentagon pairs (Thrower–Stone–Wales, see below) type transformations, (c) doping, and (d) interstitials, edges and adatoms (Figs. 12–14). While heptagon–pentagon pairs preserve the connectivity of the  $sp^2$  hybridized lattice, the interstitials and vacancies do not. Certainly, a challenge for the future will be the use of defects to design new types of MWCNTs such as helicoidal or hemitoroidal tubules, which will possess some specificity for sensing molecules or anchoring specific polymer chains.

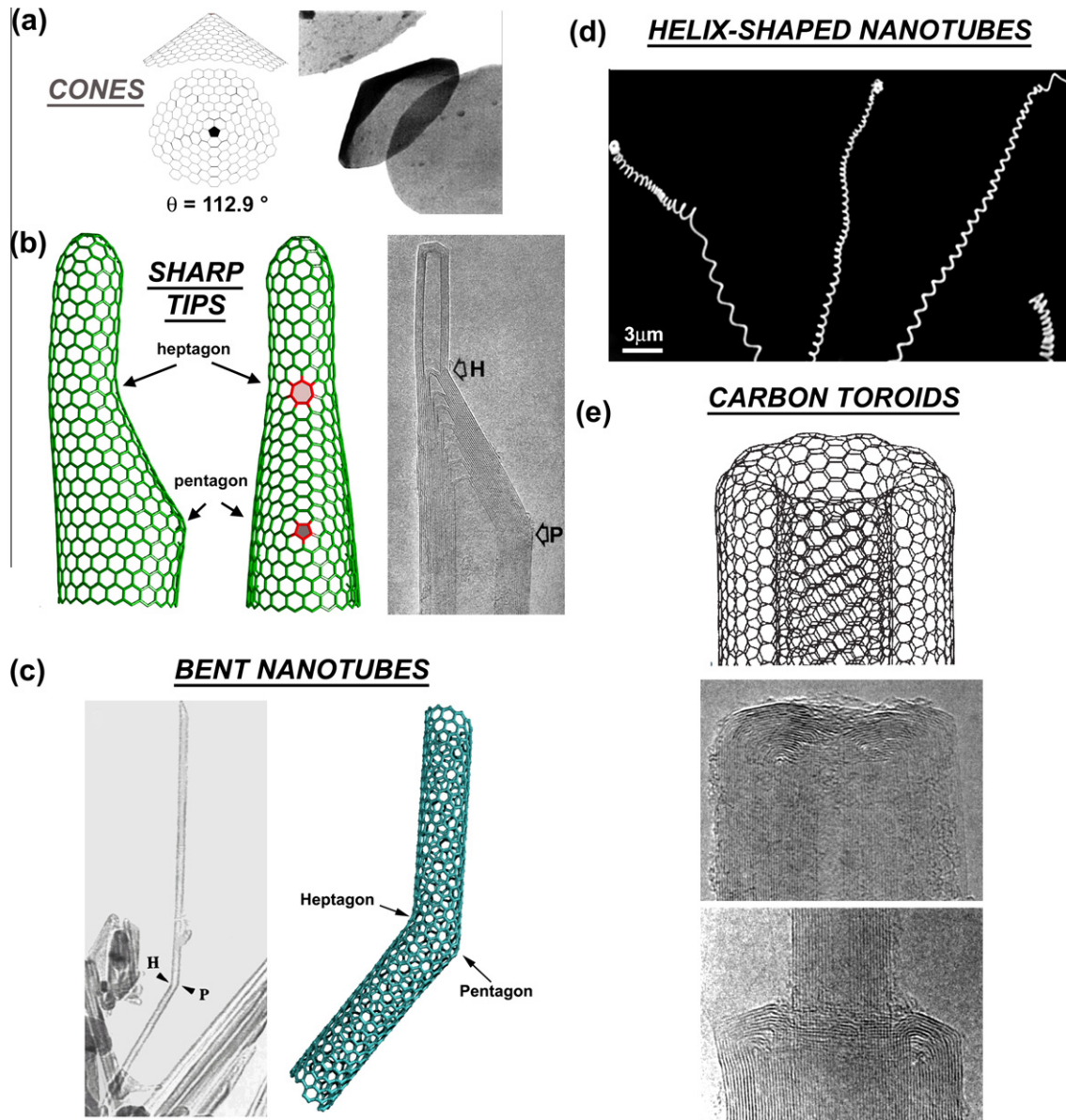


**Fig. 12** – TEM images and molecular models of different types of structural defects: (a) multi-layer graphitic cones constructed by adding one pentagon in the hexagonal carbon lattice; a molecular model and an experimental TEM image of such cones are shown for clarity (model courtesy of M. Endo, experimental image courtesy of T.W. Ebbesen; see also Krishnan et al. [102]); (b) CNT tip showing the influence of a pentagon and heptagon. The image shows the molecular models and a HRTEM image of a MWCNT displaying such structure has been reported in the literature [103]; (c) TEM image of a 30° bent MWCNT and molecular model of a bent nanotube created by adding a pentagon–heptagon pair. Only two defects result in the change of chirality and diameter of the tube before and after the kink; (d) image of carbon helices produced by the CVD process of triazine over cobalt oxide substrates [104] (see also Bandaru et al. for a discussion of coiled structures [105]); and (e) molecular model of a hemitoroidal nanotube cap, consisting of two concentric nanotubes joined together at their top rims, containing 5–7 rings, and hemitoroidal MWCNT caps found in cathode deposit (interlayer spacing approximately 0.34 nm) [101,106].

### 8.1. Structural defects

Structural defects are imperfections that significantly distort the curvature of the MWCNT. These defects are caused by the presence of pentagons, heptagons, or octagons, which are embedded in the  $sp^2$  hexagonal lattice. For example if a single or a few pentagons are embedded into the graphitic lattice, multilayer nanocones with different apex angles are ob-

tained (see Fig. 12). A 30° angle in a CNT could also be explained by the presence of pentagon on one side of the tube and a heptagon on the opposite side; similar structures have been observed for bent MWCNTs (see Fig. 12). Similarly, hemitoroidal caps have been observed experimentally in MWCNTs at high temperatures [101]. The reactivity of pentagons, heptagons or octagons with specific acceptor or donor molecules has still to be determined from the theoretical and experi-

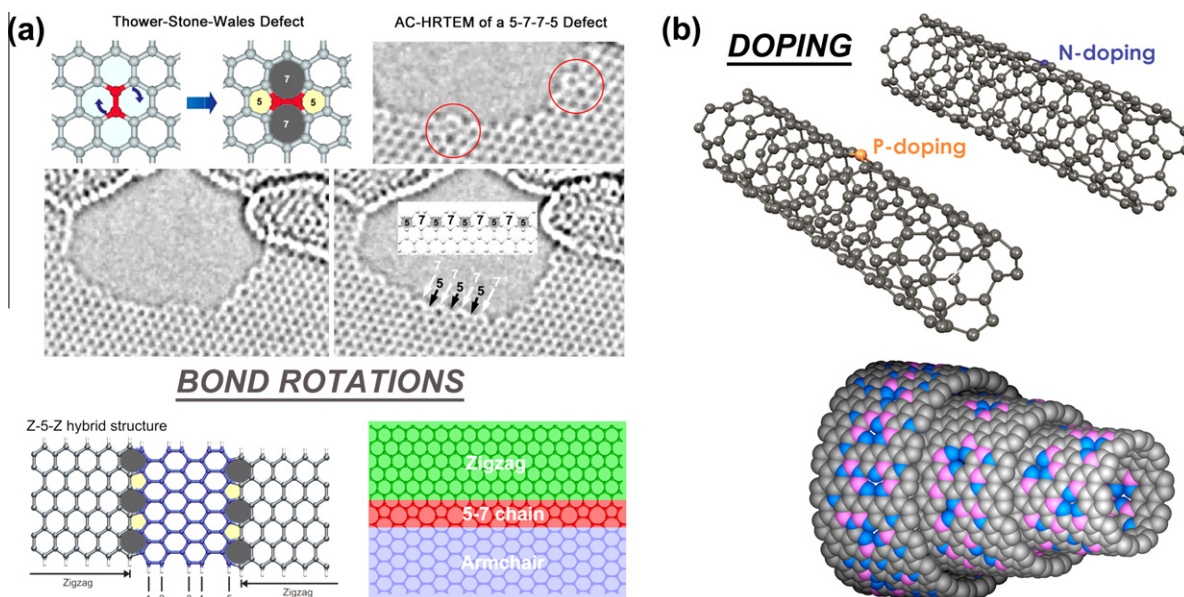


**Fig. 13 – (a) Molecular model of the Throrer–Stone–Wales defect transforming four hexagons into two pentagons and two heptagons. Next to the model, a HRTEM image showing experimentally created 5-7-7-5 defects and 57575757 lines. Below, a hybrid graphene ribbon connecting zigzag ribbons with an armchair ribbon are shown; (b) molecular models of nitrogen- and phosphorous-doped carbon nanotubes as well as a random arrangement of BCN materials within concentric tubes.**

mental standpoints, and their estimation could be achieved by use of aberration corrected HRTEM (AC-HRTEM) (see Figs. 13 and 14).

### 8.2. Bond rotations

Bond rotations occur on tube surfaces and do not result in large curvature distortions of the tubule (see Fig. 13a). In particular, these defects could be 5-7-7-5 pairs embedded in the hexagonal network or Throrer–Stone–Wales (TSW-type) defects [107,108] that could be created by rotating a carbon-carbon bond  $90^\circ$  within four neighboring hexagons, thus resulting in the transformation of two pentagons and two heptagons [109]. The authors of this review have called the 5-7-7-5 defects, Throrer–Stone–Wales defects, as a recognition to these authors. Peter Throrer [107] was the first to propose the presence of single or double pairs of 5-7 rings in graphites, and Stone and Wales were the first to propose  $90^\circ$  bond rotations in fullerenes. These combined effects result in the formation of 5-7-7-5 defects. It is noteworthy that the electronic and chemical properties of these 5-7 or 5-7-7-5 pairs (Fig. 13a) are different from the structural defects, and their reactivity and detection needs to be investigated theoretically and experimentally. Recently, Zettl and coworkers were able to directly observe 5-7 and TSW defects on isolated graphene surfaces by use of aberration-corrected transmission electron microscopy (see Fig. 13a and also see movies from Supplementary material of [110]).

### 8.3. Doping-induced defects

Doping-induced defects arise from substitutional non-carbon atoms embedded in the tubular lattice of MWCNTs (Fig. 13b).

For example, it has been shown that N and B atoms could be introduced into MWCNTs. With both dopants, the chemical reactivity of the tube surface increases, in one case due to the fact that N has one electron more than C, in the other because B has one electron less than C. Therefore, these types of defects could be used to tune the type of conduction in nanotube materials, ranging from n-type transport (substitutional nitrogen doping) to p-type conduction (substitutional boron atoms in the lattice) [111]. Recent studies have demonstrated that other elements such as P, S, Si and paired dopants such as phosphorous–nitrogen could also be introduced in the hexagonal lattice single and multiwall carbon nanotubes [112–115].

### 8.4. Non- $sp^2$ carbon defects

Non- $sp^2$  carbon defects could be present in MWCNTs and are caused by the presence of highly reactive carbon atoms such as dangling bonds, carbon chains, interstitials (free atoms trapped between graphitic sheets), edges (open nanotubes), adatoms and vacancies (Fig. 14). These defects are usually observed with HRTEM when the adsorbed atoms on these reactive sites are removed by the electron beam energy.

## 9. Concluding remarks

TEM remains the most significant tool for the researcher attempting to characterize structural properties of MWCNTs. The conservative researcher would be prudent in saying that identification of multiple tube walls is the only way to know whether MWCNTs exist in a sample batch. Extending this to HRTEM, we have presented a case for FFT as an adjunct to evaluate nanotube crystallinity and presence of defects.

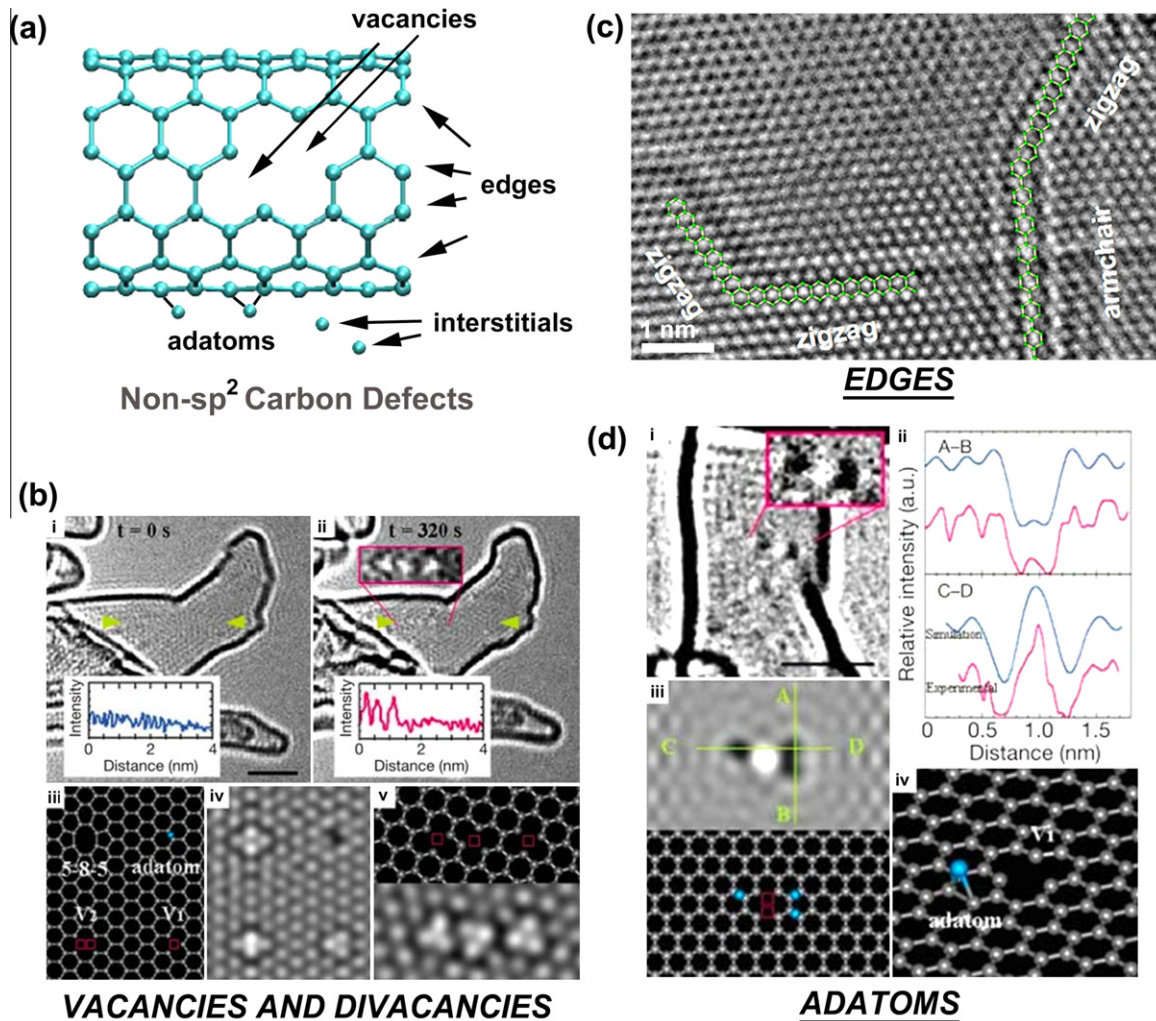


**Fig. 14** – (a) Molecular model of the different types of non- $sp^2$  defects: vacancies, divacancies, interstitials, adatoms, edges and interstitials; (b) experimental images showing the creation of vacancies in graphitic materials (bi and ii) and bii – inset, molecular models and HRTEM image simulations are also shown for clarity (bii–v; data obtained with permission from Hashimoto et al. [116]); (c) HRTEM image of graphene edges exhibiting zigzag and armchair edges, that were obtained by applying Joule heating on an individual graphene nanoribbons inside the HRTEM [117]; (di and ii) HRTEM image of adatoms on a graphitic surface (see darker contrast spots); (diii and iv) HRTEM simulations and models of different configurations of adatoms on the surface of graphene that correspond to the experimental observations. (Data obtained with permission from Hashimoto et al. [116].)

SEM is sufficient to closely approximate nanotube diameter and thus infer the presence of MWCNTs rather than, say, carbon fiber or SWCNTs. However, MWCNTs are produced in multi-ton quantities, and TEM or SEM sampling for industrial production may not be very practical. Other tools provide relevant information. Raman spectroscopy, TGA, and color provide a picture of material purity after one has established the presence of MWCNTs in a bulk sample (e.g., a pile of soot). Several authors have previously studied the influence of defects on the behavior of Raman spectra, which points to the value of Raman spectroscopy in routine evaluation as well as the need for further investigation. Density and area are quantitative measures that support very fundamental questions for making engineering and economic decisions for a given application. In general, the best way to characterize

MWCNT samples is by combining 3 or more characterization techniques. In this way, a basis for quality control for bulk production can be achieved. It is clear that reference samples characterized by standard protocols are needed. The large commercial interest and growing production of MWCNTs merits continued research.

### Acknowledgments

Thanks to Prof. M.S. Dresselhaus for helpful feedback regarding this review. M.T. thanks JST-Japan for funding the Research Center for Exotic NanoCarbons, under the Japanese regional Innovation Strategy Program by the Excellence. Thanks to Robert Keller for comments regarding imaging.

## Appendix A

According to ISO/TC 229 N 270b regarding Terminology and Definitions for Carbon Nanomaterials (Working draft for consideration in ISO/TC229/WG1); the preferred relevant terms are:

### A.1. Single-wall carbon nanotube (SWCNT)

Carbon nanotube composed of a single cylindrical graphene layer.

Note: Its structure corresponds to a graphene sheet rolled up into a seamless honeycomb structure around a cylinder.

### A.2. Multiwall carbon nanotube (MWCNT)

Carbon nanotube composed of concentrically nested multiple graphene sheets with interlayer distances similar to those of graphite.

Note: Its structure is either many single-wall carbon nanotubes nested each other or a single graphene layer rolled up like a scroll. It is cylindrical for small diameters but tends to have a polygonal cross-section as the diameter is increased.

### A.3. Double-wall carbon nanotube (DWCNT)

Carbon nanotube consisting of two concentrically nested single-wall carbon nanotubes.

Note: Although this is conceptually a kind of multiwall carbon nanotube, its properties are rather close to those of single-wall carbon nanotubes.

### A.4. Characteristics of interest

From an informal survey of vendor literature, vendor website and verbal discussion, a partial list of measurements of interest includes:

- Color.
- Purity with respect to non-nanotube carbon.
- Catalyst (amount, type).
- Bulk density.
- Ash (see ASTM D2584, D5630, ISO 3451; ash is the name given to all non-aqueous residue that remain after a sample is burned, and consists mostly of metal oxides).
- Raman scattering characteristics (D/G).
- Diameter (inner/outer), Average Diameter (TEM, Raman).
- Length, Average Length (TEM).
- Metal Oxide %, Ash (TGA).
- Amorphous Carbon – (HRTEM).
- Surface Area  $\text{m}^2/\text{g}$  (BET).
- Metal Impurities (X-ray fluorescence spectroscopy).
- Toxicity (e.g., exposure limits).

### A.5. Partial list of regulatory requirements in the US

- (1) Type of multiwalled carbon nanotube (concentric cylinders, stacked cups or scrolled tubes; number of walls/tubes).

- (2) Configuration of nanotube ends (e.g., open, capped).
- (3) Description of any branching.
- (4) Width/diameter of inner most wall/tube (average and range).
- (5) Carbon unit cell size and connectivity.
- (6) Alignment of nanotube along long axis (straight, bent, buckled).
- (7) Hexagonal array orientation used in the manufacture of the nanotube.
- (8) Particle size of catalyst used in the manufacture of the nanotube.
- (9) Molecular weight (average and range).
- (10) Particle properties: shape, size (average and distribution), weight (average and distribution), count, surface area (average and distribution), surface-to-volume ratio, aggregation/agglomeration.
- (11) Structural defect content (non-carbon impurities, lattice defects, adsorbed molecules).

## REFERENCES

- [1] Iijima S. Helical microtubules of graphitic carbon. *Nature* 1991;354(6348):56–8.
- [2] Oberlin A, Endo M, Koyama T. Filamentous growth of carbon through benzene decomposition. *J Cryst Growth* 1976;32(3):335–49.
- [3] Eklund P, Ajayan P, Blackmon R, Hart AJ, Kong J, Pradhan B, et al. WTEC International Assessment of Research and Development of Carbon Nanotube Manufacturing and Applications. Technical Report. World Technology Evaluation Center Inc.; 2007.
- [4] Ma-Hock L, Treumann S, Strauss V, Brill S, Luiz F, Mertler M, et al. Inhalation toxicity of multiwall carbon nanotubes in rats exposed for 3 months. *Toxicol Sci* 2009;112(2):468–81.
- [5] Hui P, Yuanping F, Jianyi L. Ab initio study of electronic and optical properties of multiwall carbon nanotube structures made up of a single rolled-up graphite sheet. *Phys Rev B Condens Matter Mater Phys* 2005;72(8):85415–1–5.
- [6] Kaatz FH, Siegal MP, Overmyer DL, Provencio PP, Tallant DR. Thermodynamic model for growth mechanisms of multiwall carbon nanotubes. *Appl Phys Lett* 2006;89(24):241915–1–3.
- [7] Govindjee S, Sackman JL. On the use of continuum mechanics to estimate the properties of nanotubes. *Solid State Commun* 1999;110(4):227–30.
- [8] Shenderova OA, Zhirmov VV, Brenner DW. Carbon nanostructures. *Crit Rev Solid State Mater Sci* 2002;27(3/4):227–356.
- [9] Murr LE, Guerrero PA. Carbon nanotubes in wood soot. *Atmos Sci Lett* 2006;7(4):93–5.
- [10] Bang JJ, Guerrero PA, Lopez DA, Murr LE, Esquivel EV. Carbon nanotubes and other fullerene nanocrystals in domestic propane and natural gas combustion streams. *J Nanosci Nanotechnol* 2004;4:716–8.
- [11] Dillon AC, Gennett T, Jones KM, Alleman JL, Parilla PA, Heben MJ. A simple and complete purification of single-walled carbon nanotube materials. *Adv Mater* 1999;11(16):1354–8.
- [12] Krause B, Petzold G, Pegel S, Pötschke P. Correlation of carbon nanotube dispersability in aqueous surfactant solutions and polymers. *Carbon* 2009;47(3):602–12.
- [13] Lerche D, Sobisch T. Consolidation of concentrated dispersions of nano- and microparticles determined by

- analytical centrifugation. *Powder Technol* 2007;174(1–2):46–9.
- [14] Yu J, Grossiord N, Koning CE, Loos J. Controlling the dispersion of multi-wall carbon nanotubes in aqueous surfactant solution. *Carbon* 2007;45(3):618–23.
- [15] Grossiord N, Regev O, Loos J, Meuldijk J, Koning CE. Time-dependent study of the exfoliation process of carbon nanotubes in aqueous dispersions by using UV–visible spectroscopy. *Anal Chem* 2005;77(16):5135–9.
- [16] Osswald S, Havel M, Gogotsi Y. Monitoring oxidation of multiwalled carbon nanotubes by Raman spectroscopy. *J Raman Spectrosc* 2007;38(6):728–36.
- [17] Mansfield E, Kar A, Hooker S. Applications of TGA in quality control of SWCNTs. *Anal Bioanal Chem* 2010;396(3):1071–7.
- [18] Hurst KE, Van Der Geest A, Lusk M, Mansfield E, Lehman JH. Quartz–crystal microbalance for in situ monitoring of laser cleaning of carbon nanotubes. *Carbon* 2010;48(9):2521–5.
- [19] Caplovicova M, Danis T, Buc D, Caplovic L, Janik J, Bello I. An alternative approach to carbon nanotube sample preparation for TEM investigation. *Ultramicroscopy* 2007;107(8):692–7.
- [20] Endo M, Takeuchi K, Hiraoka T, Furuta T, Kasai T, Sun X, et al. Stacking nature of graphene layers in carbon nanotubes and nanofibres. *J Phys Chem Solids* 1997;58(11):1707–12.
- [21] Banhart F, Grobert N, Terrones M, Charlier JC, Ajayan PM. Metal atoms in carbon nanotubes and related nanoparticles. *Int J Mod Phys B Condens Matter Phys Stat Phys Appl Phys* 2001;15(31):4037–69.
- [22] Endo M, Hayashi T, Kim Y-A. Large-scale production of carbon nanotubes and their applications. *Pure Appl Chem* 2006;78(9):1703–13.
- [23] Kamaras K, Pekker A, Bruckner M, Borondics F, Rinzler AG, Tanner DB, et al. Wide-range optical spectra of carbon nanotubes: a comparative study. *Phys Status Solidi B* 2008;245(10):328–31.
- [24] Theocharous E, Engtrakul C, Dillon AC, Lehman J. Infrared responsivity of a pyroelectric detector with a single-wall carbon nanotube coating. *Appl Opt* 2008;47(22):3999–4003.
- [25] Lin MF, Shyu FL, Chen RB. Optical properties of well-aligned multiwalled carbon nanotube bundles. *Phys Rev B Condens Matter* 2000;61(20):14114–8.
- [26] Saito R, Dresselhaus G, Dresselhaus MS. Electronic structure of double-layer graphene tubules. *J Appl Phys* 1993;73(2):494–500.
- [27] Brennan ME, Coleman JN, Drury A, Lahr B, Kobayashi T, Blau WJ. Nonlinear photoluminescence from van Hove singularities in multiwalled carbon nanotubes. *Opt Lett* 2003;28(4):266–8.
- [28] Musso S, Porro S, Vinante M, Vanzetti L, Ploeger R, Giorelli M, et al. Modification of MWNTs obtained by thermal-CVD. *Diamond Relat Mater* 2007;16(4–7):1183–7.
- [29] Misra A, Tyagi PK, Rai P, Misra DS. FTIR spectroscopy of multiwalled carbon nanotubes: a simple approach to study the nitrogen doping. *J Nanosci Nanotechnol* 2007;7(6):1820–3.
- [30] Kouklin N, Tzolov M, Straus D, Yin A, Xu JM. Infrared absorption properties of carbon nanotubes synthesized by chemical vapor deposition. *Appl Phys Lett* 2004;85(19):4463–5.
- [31] Garcia-Vidal FJ, Pitarke JM, Pendry JB. Effective medium theory of the optical properties of aligned carbon nanotubes. *Phys Rev Lett* 1997;78(22):4289–92.
- [32] Yang Z-P, Ci L, Bur JA, Lin S-Y, Ajayan PM. Experimental observation of an extremely dark material made by a low-density nanotube array. *Nano Lett* 2008;8(2):446–51.
- [33] Mizuno K, Ishii J, Kishida H, Hayamizu Y, Yasuda S, Futaba DN, et al. A black body absorber from vertically aligned single-walled carbon nanotubes. *Proc Natl Acad Sci USA* 2009;106(15):6044–7.
- [34] Lehman JH, Hurst KE, Radojevic AM, Dillon AC, Osgood JRM. Multiwall carbon nanotube absorber on a thin-film lithium niobate pyroelectric detector. *Opt Lett* 2007;32(7):772–4.
- [35] Jorio A, Pimenta MA, Souza AG, Saito R, Dresselhaus G, Dresselhaus MS. Characterizing carbon nanotube samples with resonance Raman scattering. *New J Phys* 2003;5:139.1–17.
- [36] Rao AM, Richter E, Bandow S, Chase B, Eklund PC, Williams KA, et al. Diameter-selective Raman scattering from vibrational modes in carbon nanotubes. *Science* 1997;275(5297):187–91.
- [37] Maultzsch J, Reich S, Thomsen C. Chirality-selective Raman scattering of the D mode in carbon nanotubes. *Phys Rev B* 2001;64(12):121407-1–4.
- [38] Jantoljak H, Salvétat JP, Forro L, Thomsen C. Low-energy Raman-active phonons of multiwalled carbon nanotubes. *Appl Phys A Mater Sci Process* 1998;67(1):113–6.
- [39] Zhao XL, Ando Y, Qin LC, Kataura H, Maniwa Y, Saito R. Radial breathing modes of multiwalled carbon nanotubes. *Chem Phys Lett* 2002;361(1–2):169–74.
- [40] Zhao X, Ando Y, Qin LC, Kataura H, Maniwa Y, Saito R. Characteristic Raman spectra of multiwalled carbon nanotubes. *Physica B* 2002;323(1–4):265–6.
- [41] Zhao X, Liu Y, Inoue S, Suzuki T, Jones RO, Ando Y. Smallest carbon nanotube is 3 angstrom in diameter. *Phys Rev Lett* 2004;92(12):1255021-1–4.
- [42] Benoit JM, Buisson JP, Chauvet O, Godon C, Lefrant S. Low-frequency Raman studies of multiwalled carbon nanotubes: experiments and theory. *Phys Rev B* 2002;66(7):073417-1–4.
- [43] Buisson JP, Benoit JM, Godon C, Chauvet O, Lefrant S. Interpretation of the low-frequency Raman modes in multiwalled carbon nanotubes. MOLECULAR NANOSTRUCTURES: XVII international winterschool euroconference on electronic properties of novel materials. *AIP Conf Proc* 2003;685:452–5.
- [44] Lefrant S. Raman and SERS studies of carbon nanotube systems. *Curr Appl Phys* 2002;2(6):479–82.
- [45] Benoit JM, Buisson JP, Chauvet O, Godon C, Lefrant S. Low-frequency Raman studies of multiwalled carbon nanotubes: experiments and theory. *Phys Rev B Condens Matter Mater Phys* 2002;66(7):073417-1–4.
- [46] Donato MG, Messina G, Santangelo S, Galvagno S, Milone C, Pistone A. Aid of Raman spectroscopy in diagnostics of MWCNT synthesised by Fe-catalysed CVD. *J Phys Conf Ser* 2007;61(1):931–5.
- [47] Santangelo S, Messina G, Donato MG, Lanza M, Milone C, Pistone A. Low-frequency Raman study of hollow multiwalled nanotubes grown by Fe-catalyzed chemical vapor deposition. *J Appl Phys* 2006;100(10):104311-1–5.
- [48] Zhao XL, Ando Y, Qin LC, Kataura H, Maniwa Y, Saito R. Multiple splitting of G-band modes from individual multiwalled carbon nanotubes. *Appl Phys Lett* 2002;81(14):2550–2.
- [49] Nanot S, Millot M, Raquet B, Broto JM, Magrez A, Gonzalez J. Doping dependence of the G-band Raman spectra of an individual multiwall carbon nanotube. *Physica E Low-Dimension Syst Nanostruct* 2010;42(9):2466–70.
- [50] Gohil S, Ghosh S. Surface enhanced Raman scattering from multiwalled carbon nanotubes at low temperatures. *Appl Phys Lett* 2010;96(14):143108-1–3.
- [51] DiLeo RA, Landi BJ, Raffaele RP. Purity assessment of multiwalled carbon nanotubes by Raman spectroscopy. *J Appl Phys* 2007;101(6):064301-1–5.

- [52] Souza AG, Meunier V, Terrones M, Sumpster BG, Barros EB, Villalpando-Paez F, et al. Selective tuning of the electronic properties of coaxial nanocables through exohedral doping. *Nano Lett* 2007;7(8):2383–8.
- [53] Endo M, Kim YA, Hayashi T, Muramatsu H, Terrones M, Saito R, et al. Nanotube coalescence-inducing mode: a novel vibrational mode in carbon systems. *Small* 2006;2(8–9):1031–6.
- [54] Fantini C, Cruz E, Jorio A, Terrones M, Terrones H, Van Lier G, et al. Resonance Raman study of linear carbon chains formed by the heat treatment of double-wall carbon nanotubes. *Phys Rev B* 2006;73(19):193408–1–4.
- [55] DiLeo RA, Landi BJ, Raffaele RP. Purity assessment of multiwalled carbon nanotubes by Raman spectroscopy. *J Appl Phys* 2007;101(6):64307–1–5.
- [56] Chakrapani N, Curran S, Bingqing W, Ajayan PM, Carrillo A, Kane RS. Spectral fingerprinting of structural defects in plasma-treated carbon nanotubes. *J Mater Res* 2003;18(10):2515–21.
- [57] Ramadurai K, Cromer CL, Dillon AC, Mahajan RL, Lehman JH. Raman and electron microscopy analysis of carbon nanotubes exposed to high power laser irradiance. *J Appl Phys* 2009;105(9):093106–11.
- [58] Saito R, Jorio A, Souza Filho AG, Dresselhaus G, Dresselhaus MS, Pimenta MA. Probing phonon dispersion relations of graphite by double resonance Raman scattering. *Phys Rev Lett* 2001;88(2):027401–1–4.
- [59] Osswald S, Flahaut E, Ye H, Gogotsi Y. Elimination of D-band in Raman spectra of double-wall carbon nanotubes by oxidation. *Chem Phys Lett* 2005;402(4–6):422–7.
- [60] Bose SM, Gayen S, Behera SN. Theory of the tangential G-band feature in the Raman spectra of metallic carbon nanotubes. *Phys Rev B* 2005;72(15):153402–1–4.
- [61] Jinno M, Ando Y, Bandow S, Fan J, Yudasaka M, Iijima S. Raman scattering study for heat-treated carbon nanotubes: the origin of a  $1855\text{ cm}^{-1}$  Raman band. *Chem Phys Lett* 2006;418(1–3):109–14.
- [62] Kim KK, Park JS, Kim SJ, Geng HZ, An KH, Yang C-M, et al. Dependence of Raman spectra G' band intensity on metallicity of single-wall carbon nanotubes. *Phys Rev B* 2007;76(20):205426–1–8.
- [63] Brunauer AS, Emmett PH, Teller E. Adsorption of gases in multimolecular layers. *J Am Chem Soc* 1938;60(2):309–19.
- [64] Do DD. Adsorption analysis: equilibria and kinetics. London: Imperial College Press; 1998.
- [65] Rouquerol F, Rouquerol J, Sing K. Adsorption by powders and porous solids, principles, methodology and applications. London: Academic Press; 1999.
- [66] Peigney A, Laurent C, Flahaut E, Basca RR, Rousset A. Specific surface area of carbon nanotubes and bundles of carbon nanotubes. *Carbon* 2001;39:507–14.
- [67] Lucio D, Laurent D, Roger G, Yasushi S, Noriko Y. KOH activated carbon multiwall carbon nanotubes. *Carbon Sci Technol* 2009;3:120–4.
- [68] Frackowiak E, Delpeux S, Jurewicz K, Szostak K, Cazorla-Amoros D, Beguin F. Enhanced capacitance of carbon nanotubes through chemical activation. *Chem Phys Lett* 2002;361:35–41.
- [69] Raymundo-Pinero E, Azais P, Cacciaguerra T, Cazorla-Amoros D, Beguin F. High surface area carbon nanotubes prepared by chemical activation. *Carbon* 2002;40:1614–7.
- [70] Raymundo-Pinero E, Azais P, Cacciaguerra T, Cazorla-Amoros D, Linares-Solano A, Beguin F. KOH and NaOH activation mechanisms of multiwalled carbon nanotubes with different structural organisation. *Carbon* 2005;43:786–95.
- [71] Jurewicz K, Babel K, Pietrzak R, Delpeux S, Wachowska H. Capacitance properties of multi-walled carbon nanotubes modified by activation and ammoxidation. *Carbon* 2006;44:2368–75.
- [72] Tsang SC, Harris PJF, Green MLH. Thinning and opening of carbon nanotubes by oxidation using carbon dioxide. *Nature* 1993;362:520–2.
- [73] Li Z, Pan Z, Dai S. Nitrogen adsorption characterization of aligned multiwalled carbon nanotubes and their acid modification. *J Colloid Interface Sci* 2004;277:35–42.
- [74] Kim SH, Mulholland GW, Zachariah MR. Density measurement of size selected multiwalled carbon by mobility-mass characterization. *Carbon* 2009;47:1297–302.
- [75] Available from: [www.nanothinkx.com](http://www.nanothinkx.com).
- [76] Available from: [www.swentnano.com](http://www.swentnano.com).
- [77] Goldstein J, Newbury DE, Joy DC, Echlin P, Lyman CE, Lifshin E. Scanning electron microscopy and X-ray microanalysis. Springer; 2003.
- [78] Pang LSK, Saxby JD, Chatfield SP. Thermogravimetric analysis of carbon nanotubes and nanoparticles. *J Phys Chem* 1993;97(27):6941–2.
- [79] Lima A, Musumeci A, Liu H-W, Waclawik E, Silva G. Purity evaluation and influence of carbon nanotube on carbon nanotube/graphite thermal stability. *J Therm Anal Calorim* 2009;97(1):257–63.
- [80] Dunens OM, MacKenzie KJ, Harris AT. Synthesis of multiwalled carbon nanotubes on fly ash derived catalysts. *Environ Sci Technol* 2009;43(20):7889–94.
- [81] Scheibe B, Borowiak-Palen E, Kalenczuk RJ. Oxidation and reduction of multiwalled carbon nanotubes – preparation and characterization. *Mater Charact* 2010;61(2):185–91.
- [82] Kowalska E, Kowalczyk P, Radomska J, Czerwosz E, Wronka H, Bystrzejewski M. Influence of high vacuum annealing treatment on some properties of carbon nanotubes. *J Therm Anal Calorim* 2006;86(1):115–9.
- [83] Huang W, Wang Y, Luo G, Wei F. 99.9% purity multi-walled carbon nanotubes by vacuum high-temperature annealing. *Carbon* 2003;41(13):2585–90.
- [84] Lin W, Moon K-S, Zhang S, Ding Y, Shang J, Chen M, et al. Microwave makes carbon nanotubes less defective. *ACS Nano* 2010;4(3):1716–22.
- [85] Born D, Andrews R, Jacques D, Anthony J, Bailin C, Meier MS, et al. Thermogravimetric analysis of the oxidation of multiwalled carbon nanotubes: evidence for the role of defect sites in carbon nanotube chemistry. *Nano Lett* 2002;2(6):615–9.
- [86] Feng Y, Zhang H, Hou Y, McNicholas TP, Yuan D, Yang S, et al. Room temperature purification of few-walled carbon nanotubes with high yield. *ACS Nano* 2008;2(8):1634–8.
- [87] Trigueiro JPC, Silva GG, Lavall RL, Furtado CA, Oliveira S, Ferlauto AS, et al. Purity evaluation of carbon nanotube materials by thermogravimetric, TEM, and SEM methods. *J Nanosci Nanotechnol* 2007;7(10):3477–86.
- [88] Peng L, Tingmei W. Ultrasonic-assisted chemical oxidative cutting of multiwalled carbon nanotubes with ammonium persulfate in neutral media. *Appl Phys A Mater Sci Process* 2009;97(4):771–5.
- [89] Kim DY, Yang C-M, Park YS, Kim KK, Jeong SY, Han JH, et al. Characterization of thin multi-walled carbon nanotubes synthesized by catalytic chemical vapor deposition. *Chem Phys Lett* 2005;413(1–3):135–41.
- [90] Don-Young K, Young Soo Y, Soon-Min K, Hyoung-Joon J. Preparation of aspect ratio-controlled carbon nanotubes. *Mol Cryst Liq Cryst* 2009;510:79–86.
- [91] Santangelo S, Messina G, Faggio G, Lanza M, Pistone A, Milone C. Calibration of reaction parameters for the improvement of thermal stability and crystalline quality of

- multiwalled carbon nanotubes. *J Mater Sci* 2010;45(3):783–92.
- [92] Moodley P, Loos J, Niemantsverdriet JW, Thüne PC. Is there a correlation between catalyst particle size and CNT diameter? *Carbon* 2009;47(8):2002–13.
- [93] Ding F, Rosen A, Campbell EEB, Falk LKL, Bolton K. Graphitic encapsulation of catalyst particles in carbon nanotube production. *J Phys Chem B* 2006;110(15):7666–70.
- [94] McKee GSB, Vecchio KS. Thermogravimetric analysis of synthesis variation effects on CVD generated multiwalled carbon nanotubes. *J Phys Chem B* 2006;110(3):1179–86.
- [95] Li H, Zhao N, He C, Shi C, Du X, Li J. Thermogravimetric analysis and TEM characterization of the oxidation and defect sites of carbon nanotubes synthesized by CVD of methane. *Mater Sci Eng A* 2008;473(1–2):355–9.
- [96] McKee GSB, Deck CP, Vecchio KS. Dimensional control of multi-walled carbon nanotubes in floating-catalyst CVD synthesis. *Carbon* 2009;47(8):2085–94.
- [97] Zhang H, Chen Y, Zeng G, Huang H, Xie Z, Jie X. The thermal properties of controllable diameter carbon nanotubes synthesized by using AB5 alloy of micrometer magnitude as catalyst. *Mater Sci Eng A* 2007;464(1–2):17–22.
- [98] Ajayan PM, Ebbesen TW, Ichihashi T, Iijima S, Tanigaki K, Hiura H. Opening carbon nanotubes with oxygen and implications for filling. *Nature* 1993;362(6420):522–5.
- [99] Yao N, Lordi V, Ma SXC, Dujardin E, Krishnan A, Treacy MMJ, et al. Structure and oxidation patterns of carbon nanotubes. *J Mater Res* 1998;13(9):2432–7.
- [100] McKee GSB, Flowers JS, Vecchio KS. Length and the oxidation kinetics of chemical-vapor-deposition-generated multiwalled carbon nanotubes. *J Phys Chem C* 2008;112(27):10108–13.
- [101] Terrones M, Terrones H. The carbon nanocosmos: novel materials for the XXI century. *Philos Trans R Soc A* 2003;361:2789–806.
- [102] Krishnan A, Dujardin E, Treacy MMJ, Hugdahl J, Lynum S, Ebbesen TW. Graphitic cones and the nucleation of curved carbon surfaces. *Nature* 1997;388(6641):451–4.
- [103] Iijima S, Ichihashi T, Ando Y. Pentagons, heptagons and negative curvature in graphite microtubule growth. *Nature* 1992;356(6372):776–8.
- [104] Lau KT, Lu M, Hui D. Coiled carbon nanotubes: synthesis and their potential applications in advanced composite structures. *Composites Part B* 2006;37(6):437–48.
- [105] Bandaru PR, Daraio C, Yang K, Rao AM. A plausible mechanism for the evolution of helical forms in nanostructure growth. *J Appl Phys* 2007;101(9):094307-1–4.
- [106] Martel R, Shea HR, Avouris P. Rings of single-walled carbon nanotubes. *Nature* 1999;398(6725):299.
- [107] Thrower PA. The study of defects in graphite by transmission electron spectroscopy. *Chem Phys Carbon* 1969;5:217–319.
- [108] Stone AJ, Wales DJ. Theoretical studies of icosahedral C60 and some related species. *Chem Phys Lett* 1986;128(5–6):501–3.
- [109] Terrones M, Terrones G, Terrones H. Structure, chirality, and formation of giant icosahedral fullerenes and spherical graphitic onions. *Struct Chem* 2002;13(3):373–84.
- [110] Girit CO, Meyer JC, Erni R, Rossell MD, Kisielowski C, Yang L, et al. Graphene at the edge: stability and dynamics. *Science* 2009;323(5922):1705–8.
- [111] Terrones M, Jorio A, Endo M, Rao AM, Kim YA, Hayashi T, et al. New direction in nanotube science. *Mater Today* 2004;7(10):30–45.
- [112] Cruz-Silva E, Cullen DA, Gu L, Romo-Herrera JM, Munoz-Sandoval E, Lopez-Urias F, et al. Heterodoped nanotubes: theory, synthesis, and characterization of phosphorus-nitrogen doped multiwalled carbon nanotubes. *ACS Nano* 2008;2(3):441–8.
- [113] Maciel IO, Campos-Delgado J, Cruz-Silva E, Pimenta MA, Sumpter BG, Meunier V, et al. Synthesis, electronic structure, and raman scattering of phosphorus-doped single-wall carbon nanotubes. *Nano Lett* 2009;9(6):2267–72.
- [114] Maciel IO, Anderson N, Pimenta MA, Hartschuh A, Qian H, Terrones M, et al. Electron and phonon renormalization near charged defects in carbon nanotubes. *Nat Mater* 2008;7(11):878–83.
- [115] Romo-Herrera JM, Cullen DA, Cruz-Silva E, Ramírez D, Sumpter BG, Meunier V, et al. The role of sulfur in the synthesis of novel carbon morphologies: from covalent Y-junctions to sea-urchin-like structures. *Adv Funct Mater* 2009;19(8):1193–9.
- [116] Hashimoto A, Suenaga K, Gloter A, Urita K, Iijima S. Direct evidence for atomic defects in graphene layers. *Nature* 2004;430(7002):870–3.
- [117] Jia X, Hofmann M, Meunier V, Sumpter BG, Campos-Delgado J, Romo-Herrera JM, et al. Controlled formation of sharp zigzag and armchair edges in graphitic nanoribbons. *Science* 2009;323(5922):1701–5.